Master's Degree Thesis in Aerospace Engineering:

Pre-design of a Space-Based Solar Panel concept transmitting high frequency energy to user spacecrafts

Supervisors

Prof. Marco FIORITI

Eng. Hervé LEGAY

Eng. Alexandre GARUS

Candidate

Pietro MONDINO

Academic Year 2023/2024

Summary

Space-Based Solar Power (SBSP) is an innovative solution for providing power to general users. The concept involves positioning one or several high-powered photovoltaic solar stations on a highly and if possible continuously sunlit orbits and transmitting the harvested energy via high frequency beam (from narrow RF up to visible domain) to the envisaged users. In the past, use cases primarily focused on ground stations, while nowadays the idea to directly supply spacecrafts on orbit is becoming more and more attractive. The present work, intended as the final product of the double master's degree program between Politecnico di Torino and ISAE-Supaero, result of the final internship at Thales Alenia Space, focuses on this last trend. Moreover, the client satellites equipped with rectennas converts the beam power into electricity for their own energy supply, eliminating the need to be equipped with solar panels for daytime operation and batteries during eclipse. This work will develop a Thales Alenia Space-France internal project aiming at designing an Orbital System for Power Production and Distribution for satellites. After defining and selecting use cases, the intricate problem of selecting the orbits for the solar power stations is tackled, meeting the criteria of continuous sun exposure and user visibility. The working frequency selection of the wireless power transfer system naturally tends towards ultra-high frequency in order to have narrow beams, minimising the sizes of antennas and rectennas. Visible frequency domain is also envisaged in order to compare benefits and drawbacks of this application. Preliminary and schematic designs of solar stations are then proposed as well as performances and efficiency of the Wireless Power Transmission (WPT).
Two different type of use cases are tackled in order to extend the SBSP application field. The former focuses on the power transmission between master and slave satellites in a LEO formation flying configuration. The latter has the objective to supply a radio-telescope on the lunar surface at visible frequencies. Here, a 86% mass reduction with respect to the traditional technology is reached, paving the way for a promising method for lunar exploration. The simulation process performed for both use cases is detailed, starting form orbit selection until mass budget calculation. Results are shown and critically analysed to pull out the appropriate conclusions.

This dissertation promises ground-breaking insight into the evolving field of SBSP. The exploration of this technology could revolutionise power supply methods for satellites and significantly improve energy management in space.

OPEN

Table of Contents

List of Tables

List of Figures

OPEN

Acronyms

LEO
Low-Earth Orbit

LLO
Low-Lunar Orbit

SBSP
Space-Based Solar Panel

GHG
Greenhouse Gas

ASCEND
Advanced Space Cloud for European Net zero emission and Data sovereignty

WPT
Wireless Power Transmission

URD
User Requirement Document

SRP
Solar Radiation Pressure

TRL
Technology Readiness Level

RF
Radio Frequency

PEC

Power Efficiency Conversion

LOP-G

Lunar Orbiter Platform-Gateway

ISL

Inter-Satellite Link

ULM

Unified Modeling Language

OOP

Object-oriented programming

EPS

Electrical Power System

HPBW

Half Power Beam Width

FNBW

First Null Beamwidth

ESA

European Space Agency

RFCS

Regenerative Fuel Cell System

NRHO

Near-rectilinear halo orbit

DoD

Depth of Discharge

Chapter 1

Introduction

In recent years, there has been a significant surge in the utilisation of wireless power transmission in various commercial space applications. This rapid expansion has highlighted the need for a clear and precise definition of power beaming as a distinct category within WPT. It can be defined as the efficient transfer of electrical energy in a point-to-point manner across free space using a directed electromagnetic beam [1]. By employing a directive electromagnetic beam, power beaming offers an efficient means of transferring electrical power over long distances. This technology represents a revolution in the way energy can be transmitted and harnessed and holds great potential for a wide range of application.
The objective of this thesis work is to explore and analyse the various aspects and implications of power beaming in space-to-space applications carrying out a pre-design phase of a Space Based Solar Power (SBSP) station in different scenarios. In other words, energy is transferred from a SBSP orbital station to a user spacecraft via electromagnetic waves following its power requirements. Therefore, in this type of application the influence of the atmosphere is left aside since both transmitter and receiver are positioned in space.
The study initially focuses on microwaves, but later considers the advantages of increasing frequency including the visible spectrum. This broader analysis allows for a deeper evaluation of power beaming technologies and the potential benefits they offer. Through a comprehensive study, feasibility, efficiency, and potential challenges associated with implementing power beaming systems in practical space scenarios are evaluated. By gaining a deeper understanding of power beaming, this work seeks to contribute to the development and advancement of this groundbreaking technology.
The following chapters delve into the fundamental principles, theoretical models, and practical considerations of power beaming. Theoretical tools are given in order to understand the use cases presented in the following. Applications' results lead to interesting conclusion on WPT feasibility in different scenarios.

Overall, this thesis work seeks to provide a comprehensive overview of power beaming within space domain. By shedding light on the underlying concepts and exploring the practical aspects, this work aims to contribute to the growing body of knowledge in this field and pave the way for future advancements and applications of power beaming technology in space missions.

1.1 Context

This work was carried out during a 6-month internship at Thales Alenia Space, a joint venture between the french company Thales Group (67%) and the italian Leonardo (33%). Dedicated to the aerospace industry, Thales Alenia Space is a manufacturer focused on the space domain: in 2022, it has been the biggest European satellite maker. It is also a major player in the field of orbital infrastructure, providing half of the pressurised volume of the International Space Station. Thales Alenia Space is at the forefront of satellite technology used for scientific, commercial, and military or security purposes. It is responsible for the design, manufacturing and delivery of end-to-end space systems for the following areas: Telecommunications, Observation, Navigation, Science and Exploration. Thales Alenia Space designs, operates and delivers satellite-based systems to respond to six missions:

- Connect people anytime, anywhere through satellite constellations (Globalstar 2, O3B, Iridium Next...);
- Secure and defend: Thales Alenia Space provides telecommunications, high resolution optical and radar instruments, ground control systems and testing and integration centers for military applications to France and other countries;
- Observe and protect: Thales Alenia Space is involved in Sentinel and Copernicus programs dedicated to Earth observation (weather, climate...) and builds Meteosat satellites.
- Explore and understand the solar system and the universe: Thales Alenia Space is strongly invested in ExoMars and BepiColombo missions, has built antennas for ALMA and components for the ISS;
- Travel and navigate: The EGNOS program aims to help airplane landings and ship navigation through narrow channels, Galileo is tomorrow's global navigation system, KINEIS is the future French internet nanosatellite constellation and KASS is the South Korean version of EGNOS;
- Digital transformation and innovation through the creation of innovation cluster and the digitisation of the production chain.

In particular, the internship on SBSP concept was led at the Research and Technology Department (DRT) of Thales Alenia Space's Toulouse site, in charge of technical monitoring and upstream studies. The aim is to anticipate future developments, mainly through feasibility studies. These studies essentially concern telecommunication payloads, architecture, antennas, signal processing, optics, microwave and radar. Project conducted within the Department of Research and Technology can be gathered into three categories, depending on the level of proficiency:

- Upstream studies: the objective is to identify the technologies and techniques that would be likely to bring a competitive advantage to Thales Alenia Space. These are often carried out in close collaboration with academic partners.
- Deepening studies: in order to consolidate the advantages and drawbacks and so as to increase the level of maturity of the technologies, while reducing the risks simultaneously. They are carried out with a goal of realisation and implementation (with or without production of simulation tools, models...).
- Support for implementation by teams developing products that could be sent into space. At this stage, the industrialisation aspects must be covered by the industrial unit, once the technical interest is demonstrated and the risks have been mitigated.

1.2 Thesis' framework

Space-to-space microwave power beaming applications represent a new trend in space research and development that emerges from the evident space-to-ground drawbacks. Over the years, a large number of studies have been carried out to assess the SBSP feasibility to power ground station on Earth. Results showed an order of magnitude of kilometres for transmission antennas' size mainly due to atmospheric losses making the concept unfeasible considering present technologies. Consequently, according to diffraction formulas detailed in the following chapter, the idea is to increase transmission frequency in order to lower antenna dimensions. Since the atmosphere blocks high-frequency microwaves spectrum, moving the application above the atmosphere seems the most reasonable way in order to avoid all the associated losses.
Furthermore, transmission distance plays a key role in antenna design: the larger the distance between the two antennas, the greater their size. For this reason, finding feasible use cases in the short term for power beaming is an hard work. Nevertheless, when two antennas are brought closer it has to be checked if applying power beaming is worth it comparing it to the present technology, i.e. solar arrays and batteries.

This thesis work relies on the preliminary design phase of a space engineering project, where the main objective is to engage in brainstorming and explore a wide range of ideas. The key focus is on conducting simple calculations using basic formulas in order to evaluate the feasibility of these ideas. The primary challenge lies in identifying the optimal use case, which necessitates having a broad and open-minded perspective. Through this meticulous process of analysis and evaluation, the ultimate goal is to determine the viability of the proposed concepts and their potential for further development.

1.3 State of the art

Space Based Solar Power has had its first hour of glory in the 1970s, following the first oil crisis [2]. The idea was to find another way to produce energy trying to make a step over fossil fuels and all the politic and economic reasons behind their market. The typical architecture of these early systems was a gigantic scale-up of a telecommunication spacecraft, with a solar array and an antenna, both with an area in the km^2 range, connected together by a huge centralised power assembly in charge of converting direct current (DC) power into radio frequency (RF). The produced power was sent on a ground station via RF link and collected for the network distribution. The technical unfeasibility of these concepts was quickly established and the return of oil prices to a more affordable level sent them into deeply dormant mode.
Why is it, then, that SBSPs resurface today as a possible alternative to terrestrial renewable energy sources? The main reasons of this resurrection are listed hereinafter:

- Technology has made progress, significantly improving the efficiency of electronic devices both in transmission and receiving chain, particularly in terms of conversion DC to RF and amplification process. These improvements have led to enhanced performance and increased efficiency in transmitting signals. Additionally, on the receiving side, rectennas (rectifying antennas) have undergone advancements, allowing for the more efficient collection of energy compared to previous methods. The REMPOWER project aims to develop a modular, flexible and lightweight rectenna capable of capturing energy at 100 GHz reaching a Power Efficiency Conversion (PEC) higher than 70%. Nevertheless, typical rectennas working in few GHz domain present conversion efficiencies in the 70% to 90% range [3].

- Reduction in launch costs have contributed to make SBSP modular systems financially more affordable. NASA's space shuttle had a cost per unit of mass launched in Low Earth Orbit (LEO) of about $54,500/kg, while SpaceX's

Falcon 9 now advertises a specific cost of $2,720/kg [4]. Thus, commercial launch has reduced the cost to LEO by a factor of 20. The potential for multiple launches and increased payload capacity enable development and deployment of SBSP systems at a more accessible price point, opened up new opportunities for its utilisation.

- The restrictions and regulations imposed to address the greenhouse effect have had a significant positive impact on the development and utilisation of SBSP systems. The recent European Green Deal aims to transform the EU into a clean, resource-efficient, and competitive economy, in line with the goals of the Paris Agreement [5]. It foresees to reduce net emission by 55% by 2030 in order to become climate-neutral by 2050. Therefore, due to its ability to harness solar energy and produce clean, renewable power, SBSP has become an attractive option to mitigate the environmental impact associated with traditional energy sources. As governments and organisations prioritise reducing greenhouse gas emissions, SBSP has emerged as a viable solution that offers clean and sustainable energy generation.

Chapter 2

Theoretical tools

This chapter aims to provide the theoretical tools applied to the subsequent chapter's case study scenarios. It will provide a good foundation for understanding the different perspectives and methods used to dig into the following use cases in more detail.

2.1 Reference frame

For orbit simulations and the following outcomes it is essential to fix the envisaged reference frame. In engineering errors are often made because of a misunderstanding of the reference frame being used. For this dissertation it is sufficient to present the following three reference frames:

- The *Earth-Centered, Earth-Fixed (ECEF)* frame is a rotating coordinate system that is fixed to the Earth. In other words, it rotates with the Earth and consequently a GEO satellite does not move with respect to it. The origin of the ECEF frame is at the centre of mass of the Earth. The X-axis points to the intersection of the Equator and the Greenwich meridian (0° longitude), the Z-axis towards the North Pole and the Y-axis is a consequence of the cross product by the right-hand rule.

- The *Earth-Centered Inertial (ECI)* frame is a non-rotating[1] coordinate system with respect to the fixed stars. The origin of the ECI frame is also at the centre of mass of the Earth: the X-axis points towards the vernal equinox, which is the direction of the Sun at the time of the spring equinox, the Y-axis

[1]Remember that "inertial" means that the reference frame does not withstand any type acceleration.

is orthogonal to the X-axis and lies in the plane of the Earth's equator, and the Z-axis points towards the North Pole.

- The *TNW* body orbital frame[2] is centred in the considered satellite, where the X-axis points in the direction of satellite's velocity vector, the Z-axis towards the same direction as the orbit's angular momentum vector (i.e. perpendicular to the orbit plane), and the Y-axis is chosen so that the (X,Y,Z) trihedral is direct.

While the first two reference frames are useful to define satellites' ephemerides[3], the latter is used to calculate visibility angles between two spacecrafts, hence azimuth and elevation.

2.1.1 Reference frame changes

Changing reference frames is a fundamental skill in engineering. The objective is to pass from a coordinate system to another thanks to what is called the rotation matrix. In other words, every vector can be represented in the second ($\mathbf{v_2}$) or first ($\mathbf{v_1}$) reference frame coordinates after being multiplied by the rotation matrix $\mathbf{R}$ or its inverse $\mathbf{R^{-1}}$, respectively.

$$\mathbf{v_2} = \mathbf{R} \cdot \mathbf{v_1} \tag{2.1}$$

$$\mathbf{v_1} = \mathbf{R^{-1}} \cdot \mathbf{v_2} \tag{2.2}$$

The rotation matrix is determined knowing the coordinate system basis in both reference frames and using the formulas here above. Hereinafter, an example is provided to help the comprehension of this delicate passage. It is necessary to introduce two matrices:

- The standard basis [$\hat{\mathbf{e_1}}$, $\hat{\mathbf{e_2}}$, $\hat{\mathbf{e_3}}$] corresponds to the second coordinate system within its reference frame;
- The standard basis [$\hat{\mathbf{x}}$, $\hat{\mathbf{y}}$, $\hat{\mathbf{z}}$] represents the second coordinate system when expressed in terms of the first reference frame.

Therefore, the rotation matrix is found as follows based on Eq. 2.1 and 2.2:

$$[\hat{\mathbf{x}}, \hat{\mathbf{y}}, \hat{\mathbf{z}}] = \mathbf{R^{-1}} \cdot [\hat{\mathbf{e_1}}, \hat{\mathbf{e_2}}, \hat{\mathbf{e_3}}] = \mathbf{R^{-1}} \cdot I_3 = \mathbf{R^{-1}} \tag{2.3}$$

[2]So called because the axes X, Y and Z are typically marked as T, N and W respectively.

[3]Generally, an ephemeris is the trajectory of natural or artificial satellites, thus the position over time.

where I_3 is the 3x3 identity matrix. Thus, the rotation matrix is equal to the inverse of the second reference frame basis expressed in the first coordinate system. Once the rotation matrix is calculated, any switch can be performed between the two reference frame.
It should be remarked that the rotation matrix physically represents the orientation of one frame with respect to another. To define it, three parameters are the minimal set required in a three-dimensional problem. Often redundant parameters are used, i.e. more than three, either in order to improve the physical insight into the transformation or to simplify some numerical analysis. The two most used mathematical representations, quaternion and Euler angles, are detailed in the following to describe the rotation between two coordinate systems [6]. The comprehension of quaternions requires to introduce the Euler axis and angle concept.

Euler axis and angles

First of all, it is necessary to recall the concept of orthogonal matrices, i.e. a real square matrix whose columns and rows are orthonormal vectors. One way to express this is $\mathbf{Q}^T\mathbf{Q} = \mathbf{I}$, where $\mathbf{Q}$ is the considered orthogonal matrix and $\mathbf{I}$ the identity one. It is essential to remark that any reference frame basis is an orthogonal matrix since is composed by orthonormal vectors. A trivial example is represented by the 3D Cartesian reference frame basis:

$$\mathbf{Q}^T\mathbf{Q} = \begin{bmatrix} 1 & 0 & 0 \\ 0 & 1 & 0 \\ 0 & 0 & 1 \end{bmatrix} \begin{bmatrix} 1 & 0 & 0 \\ 0 & 1 & 0 \\ 0 & 0 & 1 \end{bmatrix} = \mathbf{I}$$

From matrix algebra it is known that real, orthogonal matrices have one unit eigenvalue, to which the eigenvector $\mathbf{e}$ is associated[4]:

$$\mathbf{Ae} = \mathbf{e} \qquad \text{(the eigenvalue is 1)}$$

Therefore, vector $\mathbf{e}$ does not change due to the rotation represented by matrix $\mathbf{A}$ only if it occurs around axis $\mathbf{e}$. This axis is called Euler axis, and the rotation amplitude Euler angle. Considering elementary rotations around each coordinate

[4]Remember that the definition is $\mathbf{Ae}=\lambda\mathbf{e}$, where $\mathbf{e}$ is the eigenvector corresponding to the eigenvalue λ.

axis 1, 2 and 3, it can be noticed that:

$$\mathbf{A_3}(\phi) = \begin{bmatrix} \cos\phi & \sin\phi & 0 \\ -\sin\phi & \cos\phi & 0 \\ 0 & 0 & 1 \end{bmatrix} \qquad \mathbf{e} = \begin{bmatrix} 0 \\ 0 \\ 1 \end{bmatrix} \tag{2.4}$$

$$\mathbf{A_2}(\phi) = \begin{bmatrix} \cos\phi & 0 & -\sin\phi \\ 0 & 1 & 0 \\ \sin\phi & 0 & \cos\phi \end{bmatrix} \qquad \mathbf{e} = \begin{bmatrix} 0 \\ 1 \\ 0 \end{bmatrix} \tag{2.5}$$

$$\mathbf{A_1}(\phi) = \begin{bmatrix} 1 & 0 & 0 \\ 0 & \cos\phi & \sin\phi \\ 0 & -\sin\phi & \cos\phi \end{bmatrix} \qquad \mathbf{e} = \begin{bmatrix} 1 \\ 0 \\ 0 \end{bmatrix} \tag{2.6}$$

Since the trace of matrix $\mathbf{A}$ in each case is equal to $1 + 2cos\phi$, the relation between Euler angle and rotation matrix is straightforward:

$$cos\phi = \frac{1}{2}(tr(A) - 1) \tag{2.7}$$

where $tr(A)$ indicates the trace of the matrix. Therefore, the matrix $\mathbf{A}$ has the following form related to Euler axis $\mathbf{e}$ and angle ϕ parameters:

$$\mathbf{A} = \begin{bmatrix} cos\phi + e_1^2(1 - cos\phi) & e_1e_2(1 - cos\phi) + e_3sin\phi & e_1e_3(1 - cos\phi) - e_2sin\phi \\ e_1e_2(1 - cos\phi) - e_3sin\phi & cos\phi + e_2^2(1 - cos\phi) & e_2e_3(1 - cos\phi) + e_1sin\phi \\ e_1e_3(1 - cos\phi) + e_2sin\phi & e_2e_3(1 - cos\phi) - e_1sin\phi & cos\phi + e_3^2(1 - cos\phi) \end{bmatrix} \tag{2.8}$$

Or equivalently:

$$\mathbf{A} = \mathbf{I}cos\phi + (1 - cos\phi)\mathbf{e}\mathbf{e}^T - sin\phi[e\Lambda] \qquad [e\Lambda] = \begin{bmatrix} 0 & -e_3 & e_2 \\ e_3 & 0 & -e_1 \\ -e_2 & e_1 & 0 \end{bmatrix} \tag{2.9}$$

If the rotation matrix is known, it is possible to obtain the Euler axis vector from Eq. 2.7:

$$\begin{cases} e_1 = \frac{A_{23} - A_{32}}{2sin\phi} \\ e_2 = \frac{A_{31} - A_{13}}{2sin\phi} \\ e_3 = \frac{A_{12} - A_{21}}{2sin\phi} \end{cases} \tag{2.10}$$

It should be remarked that the inverse transformation, thus from rotation matrix $\mathbf{A}$ to Euler axis/angle, is non always defined since when $sin\phi$ becomes zero the Euler axis is unknown. This occurs when ϕ is a multiple of π, i.e. it is possible to reach the final configuration through at least two rotations of same amplitude but different axis. This leads to a singularity in the attitude parameterisation.

Quaternion

The Euler axis/angle drawback leads the introduction of the quaternion concept. It is a vector of four parameters linked to the Euler axis/angle values through the following relation:

$$\begin{cases} q_1 = e_1 sin\frac{\phi}{2} \\ q_2 = e_2 sin\frac{\phi}{2} \\ q_3 = e_3 sin\frac{\phi}{2} \\ q_4 = cos\frac{\phi}{2} \end{cases} \tag{2.11}$$

It can be noticed that the quaternion is normalised:

$$q_1^2 + q_2^2 + q_3^2 + q_4^2 = 1$$

The direct transformation leads to the cosine matrix $\mathbf{A}$ in quaternion terms:

$$\mathbf{A} = \begin{bmatrix} q_1^2 - q_2^2 - q_3^2 + q_4^2 & 2(q_1q_2 + q_3q_4) & 2(q_1q_3 - q_2q_4) \\ 2(q_1q_2 - q_3q_4) & -q_1^2 + q_2^2 - q_3^2 + q_4^2 & 2(q_2q_3 + q_1q_4) \\ 2(q_1q_3 + q_2q_4) & 2(q_2q_3 - q_1q_4) & -q_1^2 - q_2^2 + q_3^2 + q_4^2 \end{bmatrix} \tag{2.12}$$

Or equivalently:

$$\mathbf{A} = (q_4^2 - \mathbf{q}^T\mathbf{q})I + 2\mathbf{q}\mathbf{q}^T - 2q_4^2[q\Lambda] \qquad [q\Lambda] = \begin{bmatrix} 0 & -q_3 & q_2 \\ q_3 & 0 & -q_1 \\ -q_2 & q_1 & 0 \end{bmatrix} \tag{2.13}$$

If the rotation matrix is available, it is possible to obtain the quaternion by the inverse transformation:

$$\begin{cases} q_1 = \frac{1}{4q_4}(A_{23} - A_{32}) \\ q_2 = \frac{1}{4q_4}(A_{31} - A_{13}) \\ q_3 = \frac{1}{4q_4}(A_{12} - A_{21}) \\ q_4 = \pm\frac{1}{2}(1 + A_{11} + A_{22} + A_{33})^{\frac{1}{2}} \end{cases} \tag{2.14}$$

Here, it should be noticed that the singularly mentioned for the Euler axis/angle case is not present anymore. Even if q_4 is null, it is always possible to evaluate one of the other components of the quaternion, surely different from zero due to the normalisation constraint. Therefore, three further sets of alternatives are available

to perform the inverse transformation:

$$\begin{cases} q_1 = \pm\frac{1}{2}(1 + A_{11} - A_{22} - A_{33})^{\frac{1}{2}} \\ q_2 = \frac{1}{4q_1}(A_{12} + A_{21}) \\ q_3 = \frac{1}{4q_1}(A_{13} + A_{31}) \\ q_4 = \frac{1}{4q_1}(A_{23} - A_{32}) \end{cases}$$

$$\begin{cases} q_1 = \frac{1}{4q_2}(A_{12} + A_{21}) \\ q_2 = \pm\frac{1}{2}(1 - A_{11} + A_{22} - A_{33})^{\frac{1}{2}} \\ q_3 = \frac{1}{4q_2}(A_{23} + A_{32}) \\ q_4 = \frac{1}{4q_2}(A_{31} - A_{13}) \end{cases}$$

$$\begin{cases} q_1 = \frac{1}{4q_3}(A_{13} + A_{31}) \\ q_2 = \frac{1}{4q_3}(A_{23} + A_{32}) \\ q_3 = \pm\frac{1}{2}(1 - A_{11} - A_{22} + A_{33})^{\frac{1}{2}} \\ q_4 = \frac{1}{4q_3}(A_{12} - A_{21}) \end{cases}$$

Euler angles

Another key mathematical representation to switch between two reference frames is represented by the Euler angles. It relies on the possibility to overlap two orthogonal frames choosing an appropriate rotation sequence of one coordinate system around its reference axes. The direction cosine matrix $\mathbf{A}$ can be written by adopting the rule of consecutive rotations. Considering for instance three consecutive rotations around axes 3, 2 and 1 in this order[5]:

$$\mathbf{A_{321}}(\phi, \theta, \psi) = \mathbf{A_3}(\phi) \cdot \mathbf{A_2}(\theta) \cdot \mathbf{A_1}(\psi) \tag{2.15}$$

where $\mathbf{A_3}(\phi)$, $\mathbf{A_2}(\theta)$ and $\mathbf{A_1}(\psi)$ are the 2.6 matrices with the appropriate angle notation. The rotation matrix associated is shown hereinafter:

$$\mathbf{A_{321}} = \begin{bmatrix} cos\phi cos\theta & cos\theta sin\phi & -sin\theta \\ -cos\psi sin\phi + sin\psi cos\phi sin\theta & cos\psi cos\phi + sin\psi sin\phi sin\theta & sin\psi cos\theta \\ sin\psi sin\phi + cos\psi cos\phi sin\theta & -sin\psi cos\phi + cos\psi sin\phi sin\theta & cos\psi cos\theta \end{bmatrix} \tag{2.16}$$

[5]It should be remarked that the axes 1, 2 and 3 does not refer to any particular reference frame, but indicate the directions of the performed rotation.

The inverse transformation from matrix **A** to Euler angles takes the following form:

$$\begin{cases} \theta = -sin^{-1}(A_{13}) \\ \phi = tan^{-1}(\frac{A_{12}}{A_{11}}) \\ \psi = tan^{-1}(\frac{A_{23}}{A_{33}}) \end{cases} \tag{2.17}$$

It can be noticed that a singularity is present when $cos\theta$ is zero. This means that the first and last rotations, indicated by ψ and ϕ respectively, are actually around the same physical direction in space, therefore it is not possible to distinguish them individually.
Depending on the chosen combination of rotation axes, the rotation matrix **A** changes. Two consecutive rotations cannot be around the same axis since it would become one single rotation. Therefore the possible sequences are 12 in total[6]: 6 of them have all the indexes different while the other 6 are characterised by the same first and third index. The various sets of Euler angles are singular for different values of the second rotation angle θ: when all indexes are different, the singularity condition appears for $\theta = (2n + 1)\pi/2$, while for equal first and third index the singularity occurs when $\theta = n\pi$.

To sum up, although Euler angles have a clear physical meaning, they are numerically time consuming and hard to implement. Therefore, quaternions are preferred since they do not present any singularity in the inverse transformation from the rotation matrix. Lastly, both mathematical representations simplify for small angles, i.e. up to around 15°. This is not the case, thus the details are not presented.

[6]All the 12 matrices are not shown for simplicity but they can be easily derived form 2.6.

2.2 Antenna theory

In this section the basic principles of antennas are detailed. The goal is to give out the tools needed to understand the WPT between transmitting and receiving antenna. In this way, the radiation pattern, i.e. the directional distribution of the electromagnetic energy radiated by the antenna, is determined and consequently antenna design can be performed.

2.2.1 Radiation from apertures [7]

There are large number of antenna types for which the radiated electromagnetic fields can be considered to emanate from a physical opening or aperture. Identifying the general class of antennas is advantageous in that it provides a very convenient basis for analysis and permits a number of well established mathematical techniques to be applied to provide expressions for the distant radiation fields.
The steps involved in the analysis of aperture antennas are first to calculate the electromagnetic fields over the aperture due to the sources on the rearward side of the infinite plane and to use these field distributions as the basis for prediction of the distant fields. The electromagnetic fields in the aperture plane can rarely be determined exactly but approximate distributions can be found by a variety of methods, which are dependent upon antenna. For any antenna for which the aperture concept is valid, and for which an approximate aperture field distribution can be established, the expressions for the distant radiated fields can be formulated because the aperture and radiation fields are the Fourier transformation of each other. This concept is the basis for understanding the reasoning explained in the following. First, it is better to refresh the memory on the Fourier transformation theory.

Fourier transformation

The Fourier transformation is a powerful mathematical tool highly valuable in various fields, such as signal processing, communications, audio and image processing, and data analysis. The 1D and 2D relationships are shown hereinafter:

$$F(u) = \int_{-\infty}^{\infty} f(x) e^{-j2\pi ux}\, dx \tag{2.18}$$

$$F(u,v) = \int_{-\infty}^{\infty}\int_{-\infty}^{\infty} f(x,y) e^{-j2\pi(ux+vy)}\, dxdy \tag{2.19}$$

To make things clearer, signal processing is taken as example for Fourier transformation application. The goal is to take a signal in the time domain and converts it into a representation in the frequency domain, showing how different frequencies

contribute to the considered signal. Thus, in the expression 2.18 the variable x in the integral represents the time and the u the coordinate in the frequency domain. It is important to notice that also the inverse transformation exists, nevertheless it is not essential in the following since the goal is to determine the power radiation pattern received by the distant antenna.

Hereinafter, three main aperture types are taken into account, i.e. line source distribution, rectangular aperture, and circular one (Fig. 2.1). More complex aperture distributions can be consequently derived: since an analytical solution does not exist, a numerical solution can be performed.

An important remark has to be done to prevent any misunderstanding. The

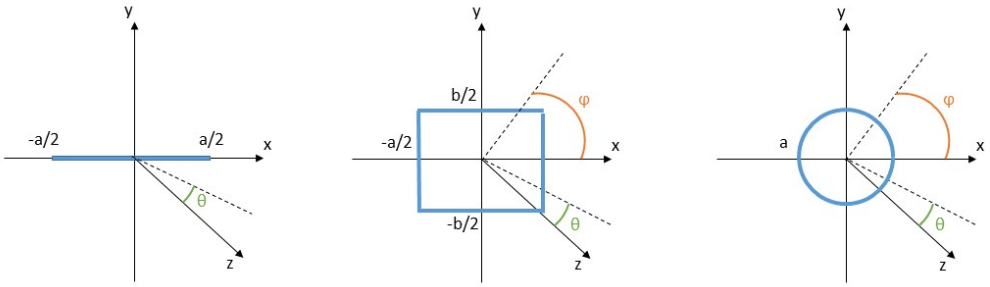

Figure 2.1: Line, rectangular and circular source apertures with the azimuth ϕ and elevation θ angles.

beamwidth, i.e. the main lobe angle of the antenna radiation pattern, is defined over all the span and not until the vertical[7]. In other words, on a plane it is twice the angle formed with the vertical.

Line source distribution

The line source is a one dimensional aperture where the field radiates from a source, length a. This configuration does have a practical realisation, namely in a long 1D array which has sufficient elements to enable it to be approximated to a continuous distribution.

In this case, the Fourier transformation becomes:

$$F(u) = \frac{1}{2\pi} \int_{-\pi}^{\pi} E_x(p) e^{jpu} \, dp \tag{2.20}$$

[7]The axe corresponding the peak value of the main lobe, commonly seen as z in three dimensions.

where $p = \frac{2\pi x}{a}$ and $u = \frac{asin\theta}{\lambda}$. $E_x(p)$ is the electric field distribution across the aperture with respect to the p variable. In a practical way, u represents the aperture adimensional coordinate and it will be useful for the following WPT study. Note that $F(u)$ is a field radiation pattern, i.e. Volt dimensions, thus the commonly used decibels conversion has to be accurate[8]. Its expression strictly depends on the envisaged application: on this purpose some considerations are drawn out in the following. Once the field distribution has been selected, the Fourier transform can be calculated and the radiation pattern consequently derived. Tab. 2.1 sums up the characteristic of some line source field distributions. It is important to highlight that the line's length is $2a$ to avoid any misunderstanding.

Distribution	**Expression**	**3 dB beamwidth**	**Level of the 1st sidelobe**	**1st zero angular position**
Uniform	1	$0.88\frac{\lambda}{a}$	-13.2 dB	$\frac{\lambda}{a}$
Cosine	$cos(\frac{\pi x}{2a})$	$1.2\frac{\lambda}{a}$	-23 dB	$1.5\frac{\lambda}{a}$
Cosine square	$cos^2(\frac{\pi x}{2a})$	$1.45\frac{\lambda}{a}$	-32 dB	$2\frac{\lambda}{a}$
Pedestal	$1-(1-0.5)(\frac{x}{a})^2$	$0.97\frac{\lambda}{a}$	-17.1 dB	$1.14\frac{\lambda}{a}$
Taylor	$cos^3(\frac{\pi x}{2a})$	$1.07\frac{\lambda}{a}$	-25 dB	-

Table 2.1: Line source distributions (length $2a$) and their properties.

The simplest distribution across the aperture is when the electric field is constant. Inserting $E_x(p) = 1$ in Eq. 2.20, a cardinal sine function[9] is obtained:

$$F(u) = \frac{sin(\pi u)}{\pi u} = sinc(\pi u) \tag{2.21}$$

The field distribution and the relative radiation patterns in watts and decibels scale are plotted in Fig. 2.2.

It should be noted that the radiation pattern peak level corresponds to 0 dB (thus 1 W or 1 V) since the power (or voltage) is dimensionless by the maximum power (respectively voltage) value. Form this reference, all the other significant points can be calculated. Namely, the level of the first sidelobe is fundamental in the aperture distribution design since the objective is to concentrate the power in the main lobe, thus reducing the sidelobe intensity. In this case, the value -13.2 dB below the peak level of the main beam is relatively high and is the main reason

[8]The conversion between decibels and watts is $[dB] = 10 \cdot \log_{10}[W]$, while $[dB] = 20 \cdot \log_{10}[V]$ from volts to decibels.

[9]Remember that the Fourier transformation of a constant function is the cardinal sinus.

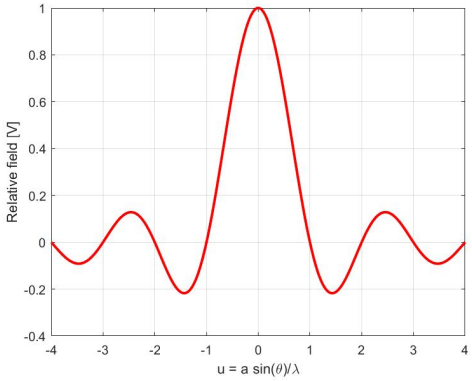

(a) Field distribution in volts of a line source with uniform illumination.

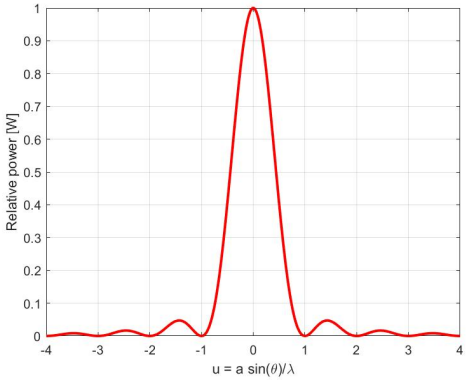

(b) Power radiation pattern in watts of a line source with uniform field distribution.

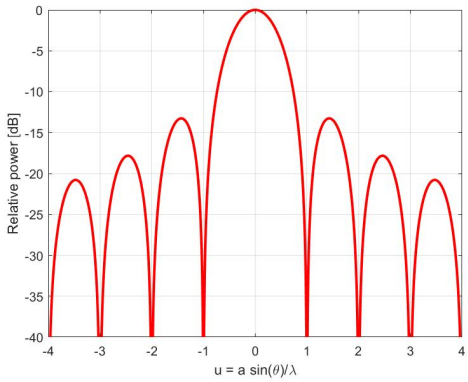

(c) Power radiation pattern in decibels of a line source with uniform field distribution

Figure 2.2: Radiation patterns of a line source with uniform field distribution.

why a uniform aperture distribution is unacceptable in a large number of antenna situations. Another important factor usually specified in antenna design is the width of the main beam. It is often expressed at the half power, or equally 3 dB. Here, the value is $0.88\lambda/a$, relatively small and thus interesting for applications. As remarked before, the abscissa value 0.88 refers to the entire angle, thus $0.44 \cdot 2$ in accordance to the beamwidth definition taken into account for this work. It is worth noting that the beamwidth is inversely proportional to the aperture size a, that is generally true for apertures operating at radio of optical frequencies. This fact is in accordance with the diffraction theory. Thinking about any kind of wave that passes towards a hole, the more the aperture is narrow, the more the divergence of the beam is higher.
As mentioned above, the high sidelobe level is a disadvantage of a uniform source distribution. This can be reduced considerably by a tapered aperture distribution where the field is greatest at the centre and reduces to a low level at the edge of the aperture. From the table it can be noted that the first sidelobe level drops at the expense of a broadening of the main beamwidth. The Taylor distribution is included as an example of an optimised distribution where the sidelobes are low and the main beam is still acceptably narrow.

Rectangular apertures

The radiation pattern of rectangular distributions can be seen as the composition of two line source distributions perpendicular to each other. For many types of antenna, such as the rectangular horn, the x and y functions are separable and the total pattern is then given by:

$$f(x, y) = f(x)f(y) \tag{2.22}$$

For cases where variables are not separable, numerical integration is probably the best solution.

Circular apertures

Circular apertures are the most common known type of antennas forming the largest single class. The paraboloidal reflector is used extremely for microwave communications and is often fed with a conical horn. The simplest form of aperture distribution is where the field does not vary with the azimuthal angle ϕ, thus is rotationally symmetric. It will be assumed in the following in order to illustrate the main features of circular apertures.
Upon integrating with respect to the azimuthal coordinate, i.e. between 0 and 2π, the following expression is obtained:

$$F(u) = \frac{2}{\pi^2} \int_0^{\pi} E_x(p) J_0(pu) p \, dp \tag{2.23}$$

where J_0 is the Bessel function of the first kind and order zero. For a uniform field distribution, i.e. $E_x(p) = 1$, the radiation pattern is:

$$F(u) = \frac{2J_1(\pi u)}{\pi u} \tag{2.24}$$

The analogy with the cardinal sine function detailed before in section 2.2.1 is evident. The sidelobe level is -17.6 dB, compared to the -13.2 dB for the line source, but the beamwidth is slightly broader at $1.02\frac{\lambda}{D}$ where $D = 2a$.

A useful aperture distribution is the pedestal that determines the level of the field at the edge of the aperture, named b hereinafter. Substituting the pedestal field expression $b+(1-p^2/\pi^2)^n$ in the equation 2.23, the following result is obtained:

$$F(u) = 2b\frac{J_1(\pi u)}{\pi u} + \frac{n!J_{n+1}(\pi u)}{(\frac{\pi u}{2})^{n+1}} \tag{2.25}$$

The expression 2.24 is obtained with $b = 0$ and $n = 0$.
Tab. 2.2 shows a number of circular aperture distribution and the corresponding radiation pattern properties. The addition of an amplitude taper reduces the level of the sidelobe and increases the width of the main beam. An important type of

Distribution $0 \leq r \leq 1$	**Expression**	**3 dB beamwidth**	**Level of the 1st sidelobe**	**1st zero angular position**
Uniform	1	$1.02\frac{\lambda}{D}$	-17.6 dB	$1.22\frac{\lambda}{D}$
Tapered to zero at edge	$1 - r^2$	$1.27\frac{\lambda}{D}$	-24.6 dB	$1.63\frac{\lambda}{D}$
Tapered to zero at edge (squared)	$(1 - r^2)^2$	$1.47\frac{\lambda}{D}$	-30.6 dB	$2.03\frac{\lambda}{D}$
Tapered to 0.5 at edge	$0.5 + (1 - r^2)^2$	$1.16\frac{\lambda}{D}$	-26.5 dB	$1.51\frac{\lambda}{D}$
Taylor	$(1 - r^2)^3$	$1.31\frac{\lambda}{D}$	-40 dB	-

Table 2.2: Circular aperture distributions (diameter D) and their properties.

circular aperture distribution is the Gaussian one. The interest relies on its Fourier transformation, that is itself of Gaussian form. Consequently, the radiation pattern does not contain sidelobes. However, a Gaussian distribution implies an infinite aperture which in practice must be truncated.

2.2.2 Gain and directivity

The power gain and directivity are quantities which define the ability of an antenna to concentrate energy in a particular direction. Introducing the spherical coordinates θ and ϕ that select a point on the aperture, the general expression of the power gain is shown hereinafter:

$$G(\theta,\phi) = \frac{4\pi \text{ power radiated per unit solid angle in direction } \theta,\phi}{\text{total power accepted from source}} \tag{2.26}$$

On the other hand, the directivity is defined in a specific direction (θ,ϕ) as follows:

$$D(\theta,\phi) = \frac{4\pi \text{ power radiated per unit solid angle in direction } \theta,\phi}{\text{total power radiated by antenna}} \tag{2.27}$$

Therefore, the difference between these two definitions relies on the radiation efficiency concept, i.e. the ratio of the total power radiated by an antenna to the net power accepted by the antenna from the connected transmitter. In other words, the power that arrives form the transmission line to the antenna terminals is higher than the real power radiated due to ohmic or dissipative losses arising from the conductivity of metal and dielectric loss. Thus, the radiation efficiency is defined with the following expression:

$$\eta(\theta,\phi) = \frac{G(\theta,\phi)}{D(\theta,\phi)} \tag{2.28}$$

which means that the directivity is always higher that the gain because does not take into account the losses.
Although power gain and directivity can be specified in any direction it is usual to refer to the peak value which coincides with the direction of the principal lobe or main beam radiated by antenna.

2.2.3 Gain and beamwidth relationship

This section is extremely important to understand the bond between power gain and beamwidth concept. First of all, it is necessary to introduce the expression that connects wavelength, gain and effective area:

$$G(\theta,\phi) = \frac{4\pi A_{eff}(\theta,\phi)}{\lambda^2} \tag{2.29}$$

It should be noted the link with the beamwidth θ that is proportional to $\frac{\lambda}{a}$ from 2.2.1. Therefore, the more the beamwidth is small, the higher is the gain. This remarkable consideration represents a pillar in the antenna domain and is summed up in the following box.

$$\theta \propto \frac{\lambda}{a} \propto \frac{1}{\sqrt{G}} \tag{2.30}$$

2.2.4 Polarisation

The polarisation of an electromagnetic wave at a single frequency describes the shape and the orientation of the locus of the extremities of the field vectors as a function of time [7]. In antenna practice the electromagnetic waves are either plane waves or may be considered as locally plane waves so that the electric E and the magnetic H fields are related by a constant called intrinsic admittance of the media of propagation:

$$H/E = \sqrt{\epsilon_0/\mu_0} \tag{2.31}$$

where ϵ_0 and μ_0 are respectively the vacuum permittivity and permeability. In these circumstances it is sufficient to specify the polarisation of the electric field vector **E** since the magnetic one can be obtained by a 90° rotation about the vector defining the direction of propagation.
The main types of polarisation are linear, circular and elliptical (Fig. 2.3). All the antennas fall into these categories or can be described from them [8].

- Linear polarisation: the E-field oscillates back and forth in magnitude staying along a single line in the wave plane[10];
- Circular polarisation: the electrical field rotates in a circle on the wave plane, thus its two orthogonal components has equal magnitude and 90° out of phase;
- Elliptical polarisation: the locus of points that the tip of the E-field vector describes is an ellipse, i.e. the perpendicular components that are out of phase by 90° are not equal in magnitude.

The field expressions function of time for all the three cases can be derived from the Maxwell's equations applying the respective boundary conditions. Nevertheless, for this thesis work scratching the surface of polarisation is enough.

Polarisation applied to antennas

In this section all the previous polarisation concepts are put in practice in antenna communication. For transmitter and receiver linearly polarised a polarisation mismatch described by the angle ϕ leads to a power loss inversely proportional to $cos^2\phi$. Therefore, a horizontally polarised antenna will not communicate with a

[10]That is the plane whose normal direction coincides with the direction of wave propagation.

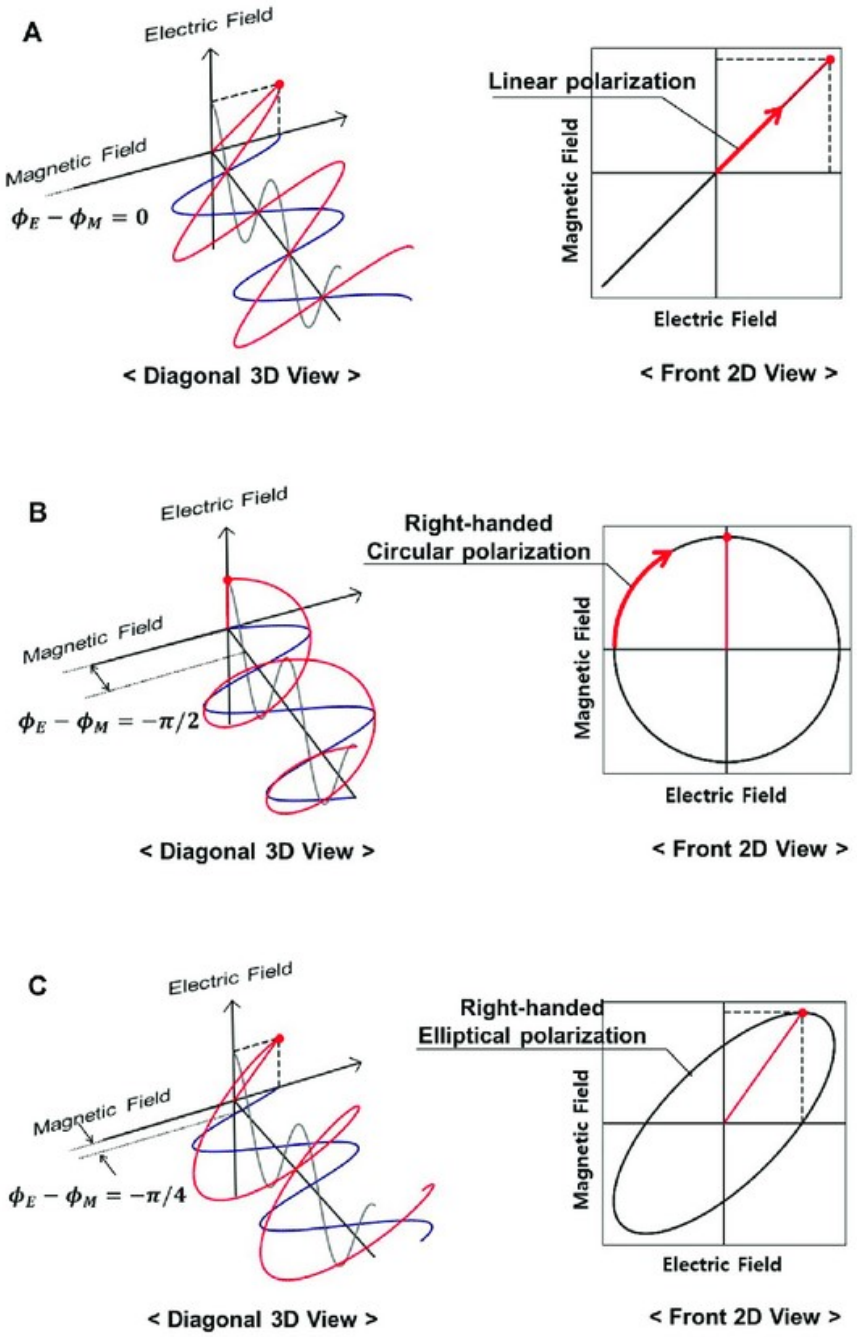

Figure 2.3: Linear, circular and elliptical polarisation types [9].

vertically polarised antenna[11]. On the other hand antennas circularly polarised do not suffer signal losses when they communicate with each other and for this reason it is a desirable characteristic for antennas. The last case to analyse is when the transmitter and the receiver have circular and linear polarisation. The linearly polarised antenna picks up the in-phase component of the circularly polarised wave. As a result, the polarisation mismatch loss will always be 0.5, i.e. 3 dB.

2.2.5 Antenna impedance and mismatch loss

Impedance Z is a fundamental concept in alternating current circuits. It measures the opposition to the current flow that a component of the circuit generates. In other words, it relates the voltage V to the current I following the Ohm's law written in a more general way at fixed time t_0:

$$V(t_0) = I(t_0) \cdot |Z|$$

The absolute value is present because impedance is generally a complex number on the form $Z = R + Xj$, where the real part R is the most known resistance while the imaginary part X is the reactance. The argument of Z, shortly $atan(X/R)$, indicates the phase shift between voltage and current. Therefore, if the resistance is zero, the impedance will be fully imaginary and the voltage leads the current by 90° in phase.
For antennas it is necessary to split the attention into two cases, low and high frequency. In short, it refers to how important is the influence of the transmission line impedance.

Low frequency

Considering low frequencies, i.e. big wavelength, the transmission line that connects transmitter (or receiver) to the antenna is short compared to a wavelength. Therefore, its influence of the circuit can be neglected. The equivalent circuit of an antenna with an impedance Z_A hooked up to a voltage source (impedance Z_S) is shown in Fig. 2.4.

The expression of the power delivered to the antenna comes from circuit theory and it is presented hereinafter:

$$P = \frac{V^2 \cdot Z_A}{(Z_A + Z_S)^2} \tag{2.32}$$

Fig. 2.5 shows the plot of Eq. 2.32 fixing source impedance Z_S at 70 Ω[12] and

[11]Remember the reciprocity theorem: antennas transmit and receive in exactly the same manner. Hence, a vertically polarised antenna transmits and receives vertically polarised fields.

[12]Typically, the source impedance is a real number.

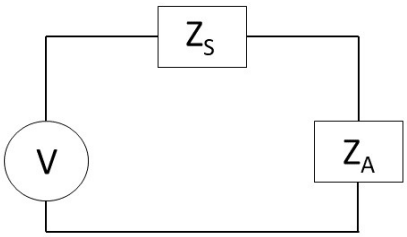

Figure 2.4: Equivalent circuit of an antenna with an impedance Z_A hooked up to a voltage source (impedance Z_S).

voltage at 1 V.

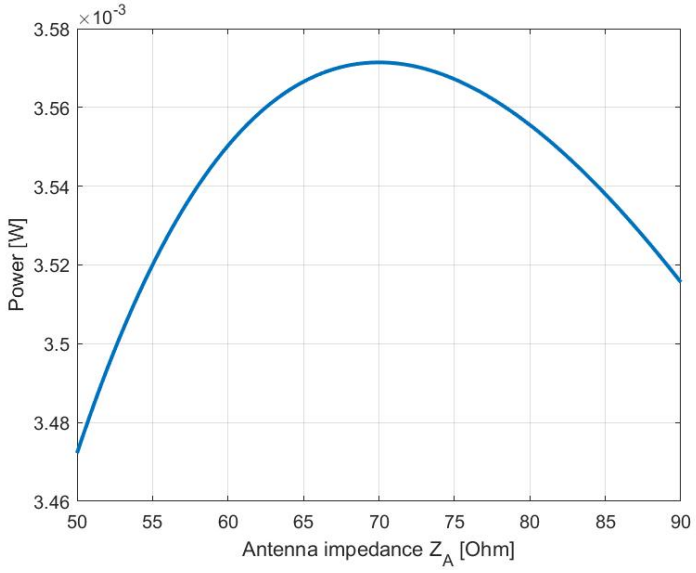

Figure 2.5: Plot of Eq. 2.32 with $Z_S = 70\,\Omega$ and voltage equals to 1 V.

It should be notice that the max power transferred is obtained for $Z_A = Z_S$. This result can be generalised for any complex number as $Z_A = Z_S^*$ where the star indicates the complex conjugate.

High frequency

Since the wavelength is shorter, the wire length becomes important and consequently the transmission line impedance Z_0 has to be taken into account. For the purpose of this work is enough to remember that if the antenna is matched to the transmission line $Z_A = Z_0$, the input impedance Z_{IN} does not depend on the length of the transmission line. Therefore, the logic will be the same as the low frequency case previously presented. This makes things much simpler: if the antenna is not matched, the input impedance will vary widely with the length of the transmission line, hence not much power will be delivered to the antenna. This power ends up being reflected back to the generator, which can cause temperature problems in itself (especially if high power is transmitted). This loss of power is known as impedance mismatch.

Two parameters are introduced hereinafter to evaluate the loss of power due to impedance mismatch: the VSWR and the S_{11} parameter.

VSWR The Voltage Standing Wave Ratio (VSWR) is a common measure of how well matched the antenna is to the transmission line or receiver. It is a real number always greater than or equal to 1. A VSWR of 1 indicates the absence of mismatch loss, i.e. the antenna is perfectly matched to the transmission line. Higher values of VSWR indicate higher mismatch loss. As an example of common VSWR values, 3.0 indicates about 75% of the power is delivered to the antenna (1.25 dB of mismatch loss). For a VSWR of 7.0, 44% of the power is delivered to the antenna, that is 3.6 dB of mismatch loss.

S_{11} parameter Generally, S-parameters describe the input-output relationship between terminals in an electrical system. For instance, taking two ports called Port 1 and Port 2, S_{12} represents the power transferred from Port 2 to Port 1. Taking about impedance mismatch, the S_{11} parameter represent the way to evaluate the power loss since it measures how much power is reflected by the antenna. For this reason it is also known as reflection coefficient or return loss.

To conclude, VSWR is clearly related to S_{11}: a VSWR of 1 corresponds to S_{11} equals to 0 dB.

2.2.6 Bandwidth

Sec. 2.2.5 contains all the information to understand the bandwidth concept, that is a fundamental antenna parameter used to describes the range of frequencies over which the antenna can properly radiate (or receive) energy. In other words it indicates all the frequencies where the mismatch loss is under a limit chosen in term of VSWR or equivalently S_{11}. Because of the antenna impedance variation with the frequency, the mismatch with the source is not always optimal. Since the source impedance is often real as mentioned before, the optimum is reached when the input impedance[13] is also real. In this particular case the antenna is said to be resonant since voltage and current are in-phase. Just to give an illustration of the orders of magnitude, an antenna operating at 100-400 MHz with a VSWR less than 1.5 (S_{11} > -13.98 dB) implies that the reflection coefficient is less than 0.2 across the quoted frequency range. Hence, only 4% of the power delivered to the antenna is reflected back to the transmitter.

[13]Remember that input impedance Z_{IN} is a general way to refer to antenna impedance taking into account the transmission line's influence.

2.2.7 WPT between antennas

This paragraph contains all the WPT basic formulas between transmitting and receiving antennas, essential to carry out the pre-design phase described in this work.
First of all, it should be noted that all the following considerations are valid beyond the Fraunhofer distance, i.e. far field range, thus when the distance between the two antennas is greater than:

$$d_{FF} = \frac{2a_{TX}^{H}a_{TX}^{V}}{\lambda} \tag{2.33}$$

where a_{TX}^{H} and a_{TX}^{V} are the two transmitting antenna's dimensions without loss of generality (equals for a circular antenna) and λ the wavelength.

It should be noted that the far field hypothesis allows to perform the small-angle approximations, thus $sin(\theta) \approx \theta$ and $tan(\theta) \approx \theta$.
At this stage, all the ingredients are provided to derive the diffraction formula. It represents a pillar for WPT antenna design since relies transmitting and receiving antenna dimensions.
First, let's consider the demonstration at FNBW for the sake of simplicity. The angular position of the first zero in the radiation pattern comes from the u definition in Eq. 2.20 applying the small-angle approximation:

$$\theta = \alpha\frac{\lambda}{a_{TX}} \tag{2.34}$$

where α is the adimensional radiation pattern coordinate u at FNBW. Fig. 2.6

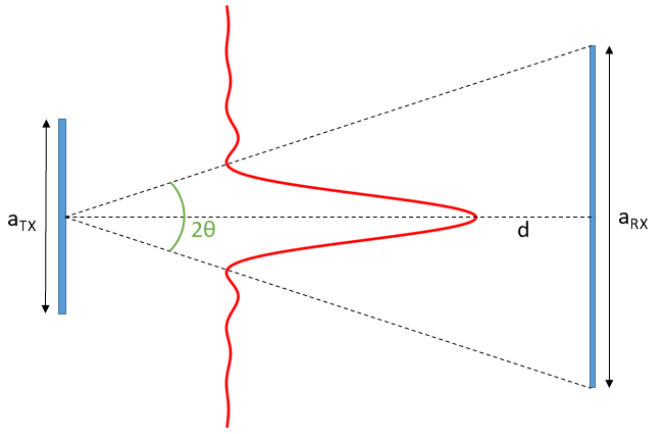

Figure 2.6: Simplified WPT configuration between transmitting and receiving antennas at FNBW.

shows the WPT configuration between transmitting and receiving antennas. The following formula can be geometrically proved taking into account the small-angle approximation:

$$\theta = \frac{a_{RX}}{d}$$

where d represents the distance between the two antennas. Substituting Eq. 2.34 in 2.2.7 the diffraction formula is finally derived:

$$a_{TX} \cdot a_{RX} = \alpha \lambda d \tag{2.35}$$

This result can be easily generalised mainly depending on two factors:

1. Illumination distribution at the transmission and the appropriate FNBW α value in Tab. 2.1 and 2.2;

2. The amount of power caught by the receiving antenna that determines the adimensional coordinate u of the field distribution.

Therefore, it is sufficient to change the α parameter adapting it to the input requirements. For instance, considering circular apertures at FNBW for both transmitting and receiving antennas, α would be 2.44, and consequently a_{TX} and a_{RX} are their respective diameters.
Finally, it is important to remark that the same concept is also valid for visible frequencies, i.e. laser emission [10]. In this case, a_{TX} and a_{RX} are respectively lens and receiving solar array dimensions. This will be useful in the following for the radio-telescope use case.

2.2.8 Radiation from arrays

The idea behind the array antenna is to put together multiple connected antennas (called radiating elements) in order to built the desired pattern. Specifically the amplitude and phase of the excitation fields on each source and the geometric spacing between them determine the output field, as if it behaves like an equivalent reflector antenna. Typical elements in arrays are dipoles, monopoles, slots in waveguides, open-ended waveguides and microstrip radiators. The choice of the type of element depends on the operating frequency and other factors such as the power handling capability, the polarisation desired, the feeding arrangements and the mechanical constraints. The array may be one dimensional with the elements in a line, forming a linear array or it may be two dimensional with the elements arranged in a rectangular or circular shape. Usually the elements are equally spaced in order to reduce the number of variables in the total design [7].
Array antennas are particularly attractive for electronic scanning where the direction

of the main beam is controlled by altering electronically the phase of the signals applied to the individual elements. These arrays are termed phased arrays. In other words the base concept is to replace mechanical steered beams using electronics: the absence of moving parts makes the system more reliable thanks to the developments in the electronic field.
A two-element array is taken into account to a better comprehension of the principal behind. Two omnidirectional sources spaced d are taken into account. The respective radiated fields are E_1 and $E_2 e^{j\delta}$, where δ indicates the phase difference between the fields. Therefore, the general expression for the far-field in the plane of the array is:

$$E(\phi) = E_1 + E_2 e^{j(\delta + \frac{2\pi}{\lambda} d cos\phi)} \tag{2.36}$$

where ϕ indicates the direction of the wave emission, thus 90° refers to the perpendicular to the array. The amplitude radiation pattern is given by the magnitude of the above equation. For example taking the same field intensity ($E_1 = E_2 = E$) and null phase difference δ, the resulting field will be $2E$ for ϕ equals to 90°. This result matches with the expectations because the waves emitted by the two elements are in phase, hence the total field magnitude doubles. To sum up the equation above proves how the resulting radiation pattern is influenced by the phase shift δ.

2.2.9 Antenna pointing accuracy

An essential parameter to take into account in antenna communication is the pointing accuracy. In other words, transmitter and receiver pointing directions are not always aligned; the angle formed defines precisely the pointing accuracy. The misalignment is due to different types of instabilities that can be summed up into attitude and orbital instabilities.

Attitude instability It refers to the inability of the satellite to maintain a desired attitude; the value mainly depends on the performance of the chosen attitude control system [11]. A value of 0.1° can be reached for a project phase 0/A as expected by this work.

Orbital instability It occurs when the satellite's orbit gradually deviates from its intended path over time. The level of the analysis relies on the type of perturbations taken into account and their influence on the considered orbit. Since the orbital instability value is complicated to predict analytically, simulations on orbital determination software programs are preferred. Finally the worst case scenario for antenna communication is represented by the max distance that occurs between transmitter and receiver over the time.

2.3 Traditional EPS sizing

As mentioned before the main goal of the SBSP concept is to remove the elements of the traditional Electrical Power System (EPS) that produce energy, hence solar array and battery. Therefore it is essential to perform a preliminary traditional EPS sizing to have a term of comparison with the new WPT technology presented in this dissertation. This subsection has the purpose to introduce the chosen method.

Solar array

First of all, the power value that the solar array must provide during daylight to supply the spacecraft for the entire orbit has to be determined. Considering d for daylight and e for eclipse, the solar array power P_{SA} in watt is given by the following first approximation formula:

$$P_{SA} = \frac{\frac{P_e T_e}{\chi_e} + \frac{P_d T_d}{\chi_d}}{T_d}$$

where P_d and P_e are respectively the power required by the satellite during daylight and eclipse in watt unit. χ_e and χ_d represent the efficiency of the paths from the solar panels through the batteries to the individual loads and the path directly from the arrays to the loads, respectively. They mainly depend on the type of power regulation methods used, but classic values are $\chi_e = 0.65$ and $\chi_d = 0.85$. Considering that the solar rays are always perpendicular to the solar panels[14], the power density in W/m^2 at the beginning of life (BOL) is defined by the following formula:

$$P_{BOL} = P_{Sun} \cdot I_d \cdot \eta_{SA}$$

where P_{Sun} is the solar irradiance equals to 1367 W/m^2 in Earth orbits, I_d the inherent degradation factor (0.95 is a typical value), and η_{SA} is the solar cell energy-conversion efficiency that depends on the chosen type. Nevertheless, it is the power at the end of life (EOL) that has to be considered to carry on a conservative design. It depends on the lifetime (in years) and the degradation level per year, both gathered in the life degradation coefficient:

$$L_d = (1 - \text{degradation})^{\text{lifetime}}$$

The annual degradation relies on the type of cells envisaged; for the most used GaAs its value is 2.75%. Consequently, the power at EOL is determined as follows

[14]Thus, the incidence losses represented by the cosine of the angle are zero.

$P_{EOL} = P_{BOL} \cdot L_d$. At this point, all the ingredients to determine the solar array area and mass are provided.

$$A_{SA} = \frac{P_{SA} \quad [W]}{P_{EOL} \quad [W/m^2]} \qquad m_{SA} = \frac{A_{SA}}{\text{specific performance } [W/m^2]}$$

Battery

Giving the battery specific energy, thus Wh/kg, the goal is to determine the battery capacity (Wh), i.e. the total amount of electrical energy a battery can deliver over a specific period, in order to find the final mass. At this stage it is necessary to introduce the concept of depth of discharge (DoD), that is the the percent or fraction of the cell or battery capacity removed during a discharge. In other words, the greater the depth of discharge on a regular basis, the sooner the cell will fail to deliver the necessary voltage for the time period required. Therefore, the spacecraft lifetime and the orbit type have a strong influence on DoD value since it decreases the higher is the number of cycles. Fig. 2.7 shows an example of DoD trend with respect to the cycle life. For instance in GEO missions, where only 100 cycles

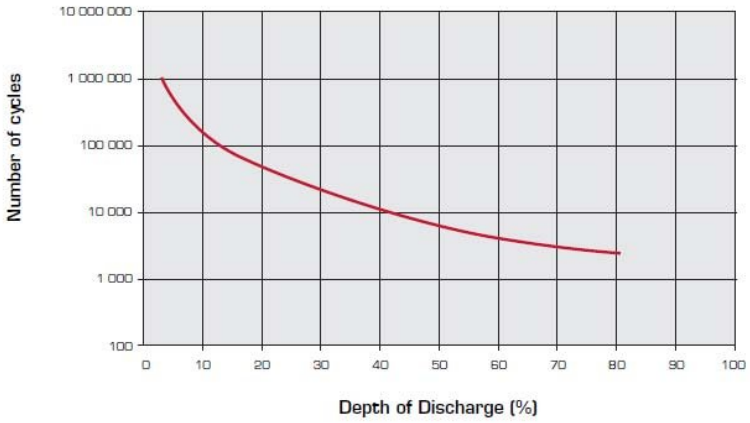

Figure 2.7: Cycle life vs. DoD for Intensium Flex High Energy Li-Ion battery, SAFT Company [12].

per year are required, the battery DoD can be high (as much as 75%); for a LEO mission requiring 5000 cycles per year, the DoD usually is well below 30%.
Setting η as the transmission efficiency between battery and load, all the ingredients to understand the battery capacity formula are given:

$$C_{battery} = \frac{P_e \cdot T_e}{DoD \cdot \eta} \tag{2.37}$$

Remember that the battery has to deliver power only during eclipses in nominal operations, hence only eclipse terms are taken into account. Now it is straightforward to find the battery mass:

$$m_{battery} = \frac{C_{battery}}{\text{specific performance [Wh/kg]}} \tag{2.38}$$

Chapter 3

Use Cases

In this chapter, SBSP applications are presented in order to provide practical examples of how a technology can be employed in real-world situations, making them a valuable tool for understanding the technology's potential and benefits. Two use cases of different nature are presented: the former is the power transmission between master and slave satellites in a LEO formation flying configuration; the latter has the objective to supply a radio-telescope on the lunar surface. The purpose of both studies is to assess the entire SBSP technology in different situations, evaluating the efficiency chain and detailing the power and mass budget. The conclusion are drawn comparing the SBSP technology with the traditional one, i.e. solar array and battery.

Hereinafter, the simulation process performed for both use cases is detailed, starting form orbit selection until mass budget calculation. Results are shown and critically analysed to pull out the appropriate conclusions.

3.1 Orbital mechanics

Orbit simulations for the first use case have been performed developing a first version of a MATLAB®[13] code, mainly focused on orbital mechanics. In the second version, power beaming considerations are added, and power and mass budget are performed, adapting it to SBSP purposes.

The hypothesis taken into account in the orbit simulator are listed hereinafter:

- The orbits are keplerian, i.e. perturbations such as atmosphere, solar radiation pressure and gravitational and magnetic anomalies are not taken into account;
- The Earth is considered as a sphere of radius $R_T + h_{atm}$, where R_T is the

earth's radius at the equator (6378 Km) and h_{atm} the atmosphere's altitude considered equals to 120 Km. This because the eventual losses of Inter-Satellite Link (ISL) crossing the atmosphere at high frequency would be enormous. Consequently, the visibility between SBSP station and user can be directly calculated with simply geometrical considerations.

The ULM (Unified Modeling Language) diagram shown in Fig. 3.1 gives a visual representation of the entire simulator (second version included). The

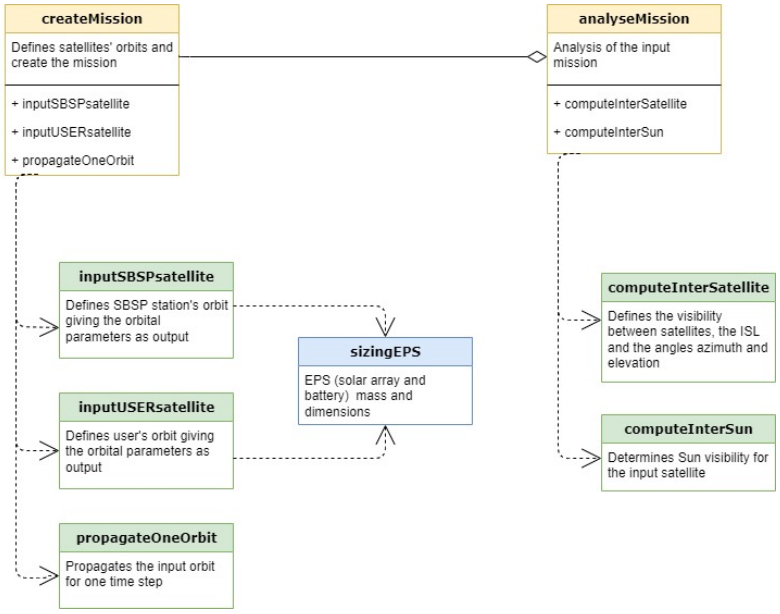

Figure 3.1: ULM diagram of the developed simulator.

general structure with main code and functions reminds that of Object-oriented programming (OOP) although it does not properly belongs to OOP category. In particular, the hole simulator is divided in two main parts: the creation (called `createMission`) and the analysis (`analyseMission`) of the mission.

- `createMission` defines the satellites' orbit calling two functions:
  - `inputSBSPSatellite` creates the SBSP station's orbit and stores all the information in a file *.cst*;
  - `inputUserSatellite` where the user's orbit is defined and stored in a *.orb* file.

Additionally, `sizingEPS` is nested in both functions giving a preliminary traditional EPS sizing with the formulas detailed in Sec. 2.3. Tab. 3.1 sums up the values used for the EPS dimensioning and gives typical magnitudes for spacecraft lifetime

in different orbit types. Finally, the curve in Fig. 2.7 has been fitted for the DoD selection in the battery design.

Lifetime [yrs]	
LEO	5
MEO	10
GEO	15
Solar array	
Efficiency [-]	0.35
Specific power $[kg/m^2]$	10
Battery	
Transmission efficiency [-]	0.95
Specific capacity $[Wh/kg]$	150

Table 3.1: Chosen values for EPS dimensioning.

After selecting the simulation time, orbits are propagated thanks to the propagator `propagateOneOrbit` and the respective ephemerides are stored in two different matrices. The final mission data are saved in a *.con* file.

- `analyseMission` takes the *.con* file as an input and performs different type of calculations useful to drawn out the sought results and the consequent conclusion:

  - taking the ephemerides of two satellites `computeInterSatellite` defines the ISL vector (hence the visibility) over the time in direction and module, and the pointing angles azimuth and elevation with respect to the TWN reference frame centred on the SBSP satellite;
  - `computeInterSun` computes the Sun visibility over the time for the considered satellite.

It is worth noting the angle criteria used to determine the SBSP station's visibility with user or Sun. Fig. 3.2 shows the condition to have satellites visibility (the logic behind Sun visibility concept is the same): angle β[1] is greater than β_{min}. In other words satellites can see each other since the whole line of sight is above the atmosphere limit.

[1]It has been calculated with scalar product definition, hence $\mathbf{R_{Sat1}} \cdot \mathbf{R_{ISL}} = R_{Sat1} R_{ISL} \cos\beta$ where R_{Sat1} and R_{ISL} are respectively the distance of the first satellite from the Earth and the inter-satellite distance.

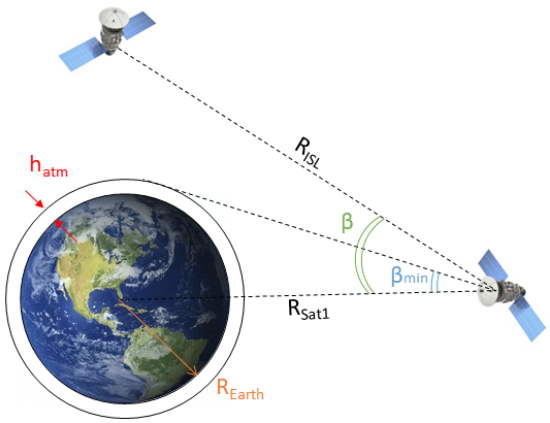

Figure 3.2: Angle criteria for satellites visibility.

3.2 Pointing angles

Pointing angles refer to azimuth and elevation values that the antenna has to follow in order to establish the optimal link. In other words, the delivered power is conceptually maximum since pointing losses are dropped. These angles are calculated with respect to the body reference frame centred in the SBSP station. Therefore, it is necessary to express the ISL vector[2] in the body coordinate system switching from *ECI* reference frame (see Sec. 2.1.1). Following the body reference frame notation detailed in Sec. 2.1, the elevation θ is the angle between the ISL vector and the **N** axis, while the azimuth ϕ is determined from the ISL vector projection in the **T** and **W** plane. At this stage it is important to clarify the chosen sign convection (Fig. 3.3): θ is positive towards the **N** direction, while ϕ towards **W**.

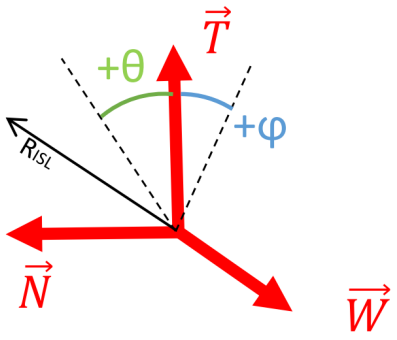

Figure 3.3: Azimuth and elevation sign convection with respect to the body reference frame.

3.3 Pointing errors

Pointing errors measure how distant is the implemented model from the reality due to perturbations. Here, the reality is represented by simulations run on GMAT software [14]. The perturbations taken into account are listed and detailed hereinafter.

Solar radiation pressure GMAT uses a simplified model called the Cannonball radiation pressure [15]. It is the simplest way to approximate the SRP acceleration

[2]The vector that relies the SBSP station to the user.

and is commonly used in preliminary mission analysis as it gives a first order approximation on the SRP impact. This model considers the SRP acceleration to be constant along the Sun-spacecraft direction, where the acceleration magnitude depends on the area-to-mass ratio and a reflectivity coefficient C_r. The total SRP acceleration is given by:

$$\mathbf{a_{SRP}} = \frac{P_{SRP} C_r A}{m} \mathbf{r_s}$$

where A is the projected area, m is the spacecraft mass, $\mathbf{r_s}$ is the normalised Sun-spacecraft direction and $C_r \in [1, 2]$ accounts for the reflectivity properties. The C_r value is hard to predict but it can be approximately equal to $1 + \rho_s$. Therefore, $C_r = 1$ indicates that all the sunlight is absorbed, while $C_r = 2$ means that all the light is reflected and twice the force is transmitted to the spacecraft.

Atmospheric drag The model used by GMAT is called MSISE-90. It is an empirical model of the atmosphere's temperature and composition valid until 700 km altitudes [16]. It is based on mass spectrometer data from various satellites and on incoherent scatter radar data from several sites.

Earth gravitational effect In particular, the zonal harmonic coefficient J_2 of the gravitational potential function plays a major role. It accounts for the deviation of the Earth's shape from a perfect sphere due to its oblateness.

n-body effect It refers to the gravitational influences of celestial bodies such as the Moon and the Sun on the spacecraft's trajectory.

It should be pointed out that the influence of this parameters depends on the orbit type. For instance, in LEO orbits solar radiation pressure plays a minor role compared to atmospheric drag, while increasing the altitude the situation is reversed.
Azimuth and elevation values at the output of the GMAT simulation are compared with the angles coming from the MATLAB® code and pointing errors are finally determined.

3.4 WPT efficiency

In the ideal case, i.e. when the two antennas are perfectly facing each other, the WPT efficiency taken into account is when the first lobe is caught. This corresponds to a efficiency value of 81.5% for a rectangular aperture (see Fig. 4.4 in the next chapter). The power relied in sidelobes is lost, hence 18.5%. Then, adding pointing errors, the visibility between the antennas is no more optimal and the efficiency

is reduced. The way depends on the chosen antenna type: the more the antenna gain is high (directive antenna), the more the WPT efficiency is influenced by pointing errors. Fig. 3.4 shows antenna directivity influence on efficiency adding pointing errors. The calculations have been performed with 100 GHz frequency considering 50 cm (high directivity) and 5 cm (low directivity) antenna dimension. As explained before, increasing the pointing error, efficiency decreases more rapidly for high directivity antennas.

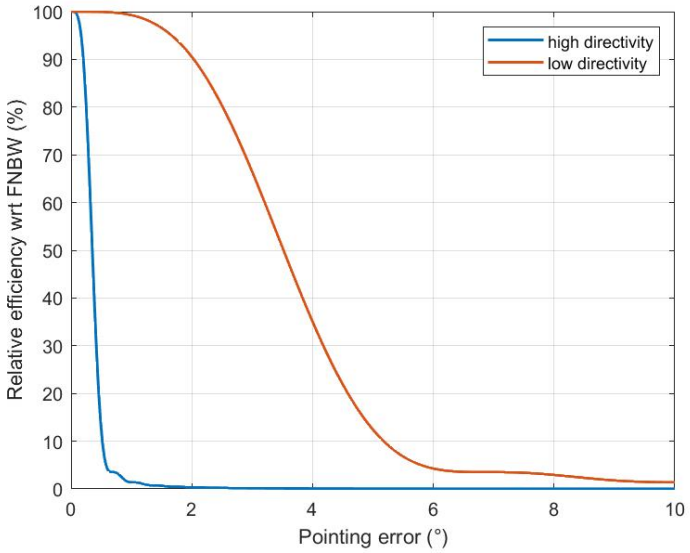

Figure 3.4: Pointing error influence over relative efficiency (wrt FNBW that is 81.5%) varying the directivity of the antenna.

Nevertheless, high gain transmitting antennas allow to reduce receiving antennas' size, therefore it is preferred to increase orbit determination model performances to lower pointing errors.

3.5 Antenna design

Antenna design relies on Eq. 2.35 since all the envisaged use cases are beyond the Fraunhofer field. Depending on the data available, different outputs can be found. Hereinafter, the wavelength, the WPT efficiency and the distance are fixed; therefore, transmitting and receiving antenna design is performed. Then, the found dimensions are checked taking into account technological and space constraints applied to the satellite.

3.6 Power sizing

The final goal is to assess the benefits adding a SBSP station to supply users via WPT. Conditions and modalities depend on the considered use case and are detailed in each following chapter. Generally, the objective consists of lowering users' EPS mass reducing solar arrays' size and battery capacity or eventually removing them. Therefore, it is essential to perform EPS sizing to understand the SBSP gain in term of mass following the procedure detailed in Sec. 2.3. Tab. 3.2 and 3.3 list the parameters' values of the solar arrays and battery chosen for the first order sizing.

Solar array (3 junction GaAs)	
Efficiency	0.35
Inherent degradation factor	0.95
Transmission efficiency SA-load	0.85
Transmission efficiency SA-battery	0.65
Degradation rate	2.75%
Area density	$10\frac{kg}{m^2}$

Table 3.2: Triple-junction GaAs solar array data.

Li-ion battery	
Energy density	$150\frac{Wh}{kg}$
Transmission efficiency battery-load	0.95
DOD (in LEO orbit)	35%

Table 3.3: Li-ion battery data.

Chapter 4

LEO-Telecom satellite system

Thales Alenia Space's project LEO-Telecom satellite system is a constellation providing a global land and ocean 5G coverage. In particular, the aim is to add a 5G coverage extension to a 5G satellite constellation in order to meet the user profiles and coverage areas requested in the URD. Hereinafter, a Thales Alenia Space's PhD study on this LEO-Telecom constellation is taken into account as use case. The goal is to split one satellite into seven, respectively one master and six slaves, in order to increase system's communication performances. Fig. 4.1 shows the general idea behind this project.

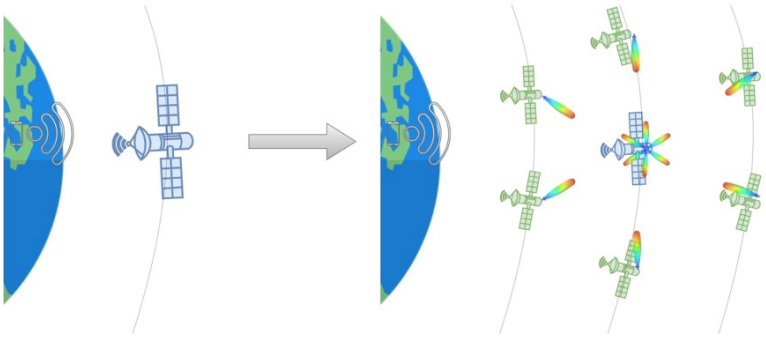

Figure 4.1: Thales Alenia Space's PhD study on LEO-Telecom constellation.

The work explained hereinafter aims to assess WPT system from the master in order to remove slaves' solar arrays and batteries. In other words the master acts as a SBSP station to supply slave satellites with the required power. This study has been performed at three distances (50 m, 100 m, and 200 m) giving a preliminary design of the rectenna as an output inter alia. It should be remarked

that the same transmitting antenna used for communication operates the WPT at the chosen frequency of 100 GHz. Pointing angles such as azimuth and elevation are detailed to orient the satellite in the right way. Pointing instabilities are taken into account in order to determine orbit control specifications.

4.0.1 Orbit

The LEO-Telecom mission aims to put 600 satellites in phased LEO orbits of 600 km altitude and 53° inclination. For the purpose of this dissertation it is sufficient to focus on just one satellite orbit, with RAAN equals to 0° for simplicity.
The PhD development configuration foresees to place slave satellites on a circle spaced by 60° around the master. It should be noticed that the distance between master and the slaves set on the nearby orbits changes over the time, being maximum at the equator and decreasing towards the poles. The value becomes null when the orbits cross; therefore the slaves changes side with respect to the master until the next crossing. Fig. 4.2 helps the visualisation of the use case.

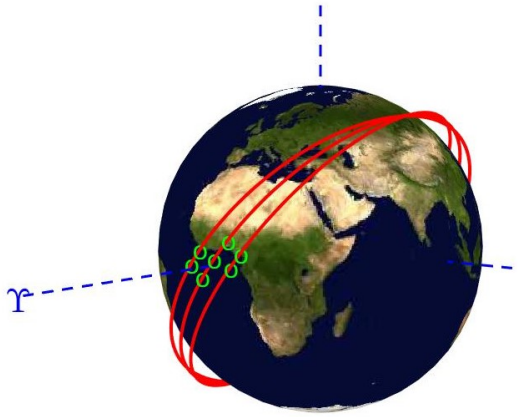

Figure 4.2: LEO-Telecom orbits in *ECI* reference frame (γ indicates the vernal point) in red, master and slave satellites in green.

It should be remarked that the considered distances between master and slaves, i.e. 50 m, 100 m, and 200 m, are measured at the equator where the maximum value logically occurs.
The general orbit properties are summed up in Tab. 4.1. Since master and slaves' orbits are relatively closed their characteristics do not show essential changes for the following study.

Altitude	600 km
Inclination	53°
RAAN	0°
Period	96.68 min 35.46 min (eclipse)

Table 4.1: Orbit properties for LEO-Telecom mission.

4.0.2 Transmitting antenna

The transmitting antenna design is based on the TACAN antenna used by military aircraft. A preliminary design of this antenna for LEO-Telecom satellites has been made: the cylinder diameter is 0.5 cm, while its height is equal to 5 cm. From the rectenna point of view, this antenna can be seen as a rectangular aperture with the cylinder dimensions just mentioned. This assumption has been carried out to simplify the WPT study between master and slave.

4.0.3 Radiation efficiency and receiving antenna design

In this section the steps to find the radiation efficiency, i.e. the amount of power collected by the receiver, are detailed. Remember that the general objective is to get the total efficiency of the entire RF chain where the radiation one is only a part of it.
First, the radiation pattern of a rectangular aperture with uniform field distribution is determined thanks to the concepts inherited from Sec. 2.2.1. It comes from the composition of two line source distributions with constant illumination as well. In this simple case the x and y functions are separable and the pattern in the principal xz plane is determined from a line source distribution *f(x)* while the pattern in the yz plane from a line source distribution *f(y)*. Therefore the field distribution $F(u, v)$ over the rectangular aperture is the following:

$$F(u, v) = F(u) \cdot F(v) = \frac{sin\pi u}{\pi u} \cdot \frac{sin\pi v}{\pi v} \tag{4.1}$$

To get the power distribution both the field function are squared. The pattern of the considered rectangular aperture is shown in Fig. 4.3.

Fig. 4.4 shows the 2D integral calculated over the function, thus the power that reaches the receiving antenna. Since the integral over all the domain is equal to one, the radiation efficiency is easily determined. The significant values Half Power Beam Width (HPBW) and First Null Beam Width (FNBW) (for u equals to 0.44 and 1 respectively as shown in Tab. 2.1) are displayed.

The receiving antenna design is based on the formulas explained in Sec. 2.2.7. The objective is to perform a trade off between the antenna size and the radiation efficiency: the more the power collected increase, the more the antenna dimensions grow.

It is interesting to notice the influence of the transmitting antenna field distribution on the receiving antenna size. This effect is shown in Fig. 4.5, dimensioning the receiver at HPBW with a transmission distance of 50 m. As mentioned in Sec. 2.2.1, the general rule foresees a reduction of the beamwidth value at the expense of the sidelobe level that increase. The Taylor field distribution tries to optimise the trade off. Furthermore, by altering the distribution of the source field, the power

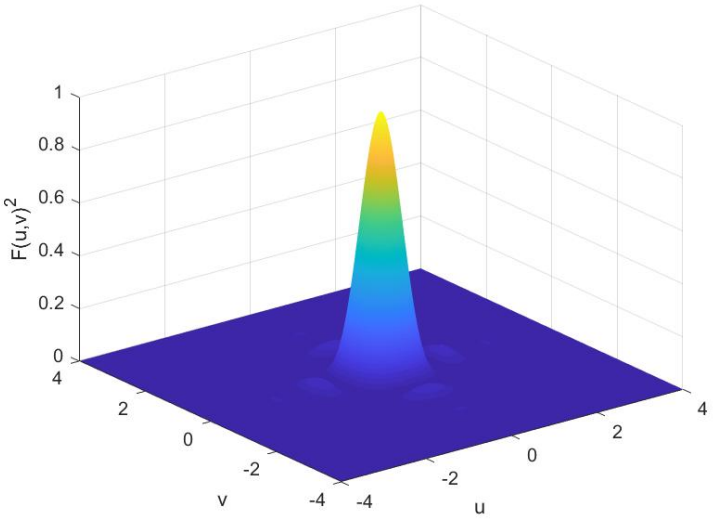

Figure 4.3: Rectangular aperture radiation pattern with constant illumination.

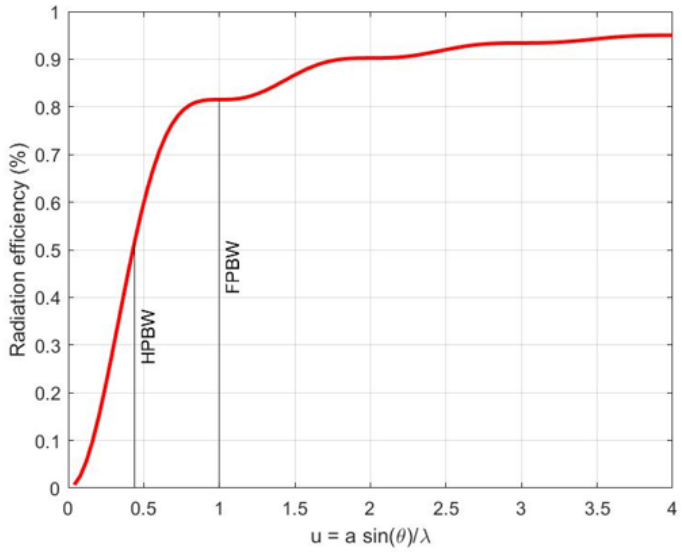

Figure 4.4: Integral of a rectangular aperture radiation pattern with constant illumination, i.e. radiation efficiency.

in the first lobe will be adjusted, thereby affecting the transmission efficiency of the WPT link.

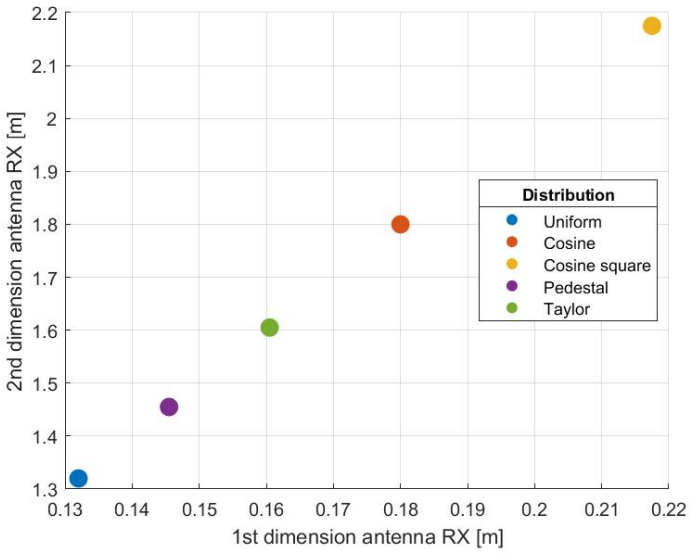

Figure 4.5: Receiving antenna dimensions varying the transmitting antenna field distribution at HPBW and at a distance of 50 m.

4.0.4 Antenna pointing accuracy

The path to find the pointing accuracy value relies on the considerations made in Sec. 2.2.9. While for attitude instability a common value of 0.1° has been chosen without much thought, for orbital instabilities the determination has been much harder. Simulations are run on GMAT software taking into account the following perturbations: SRP, atmospheric drag and gravitational harmonic coefficient J_2.

4.1 Results

The following results come from the code explained in Sec. 3.1. It should be remarked that the final objective is to compare pros and cons of the SBSP concept with the traditional EPS technology, drawing out the appropriate conclusions.

4.1.1 Sun visibility

Sun visibility represents an essential parameter to perform the traditional EPS sizing as seen in Sec. 2.3. It should be noticed that in this case all the seven

satellites have the same value since the distance between them is relatively short. Running the simulation for one year to catch all the variations due to the Earth's orbit (see Appx. A), the satellites see the Sun 67.4% of the time. Fig. 4.6 shows Sun visibility evolution over the orbit for a 1-day simulation: 1 means that visibility is checked, 0 otherwise.

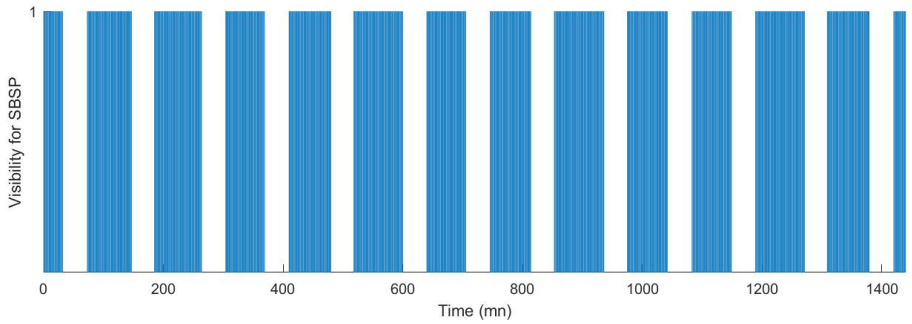

Figure 4.6: Satellite's Sun visibility over the orbit for one day simulation (1440 minutes).

4.1.2 Pointing angles

Pointing angles are determined from the consideration made in Sec. 3.2 applied to the LEO-Telecom project. Fig. 4.7 illustrates azimuth and elevation with respect to the body reference frame centred on master satellite. The shown satellites' numbering is used hereinafter to simplify the discussion.

It should be noticed that the considered distances between the orbits are small, thus orbit perturbations should not be intense and consequently do not differ much fro differences with the reality.

Azimuth

Fig. 4.8 shows azimuth angle for all the slave satellites at 50 m distance. The values are according with what happens in the reality and consequently validated. It should be remarked that the slave satellites placed in a shifted orbit with respect to the master's one (satellites 3, 4, 6 and 7) exchange positions after the crossing between the orbits near the poles. Therefore, the angle value changes appropriately sign: azimuth associated to satellites 3 and 7 oscillates between $-60°$ and $60°$, while the range for satellite 4 is $[120°, 180°]$ (same for satellite 6 but with opposite sign).

First of all, it should be observed that the azimuth value for satellite 2 and 5 is not exactly $0°$ and $180°$ respectively, but it slightly derives due to numerical issues. For the other slave satellites note that angle oscillations are related to the orbit

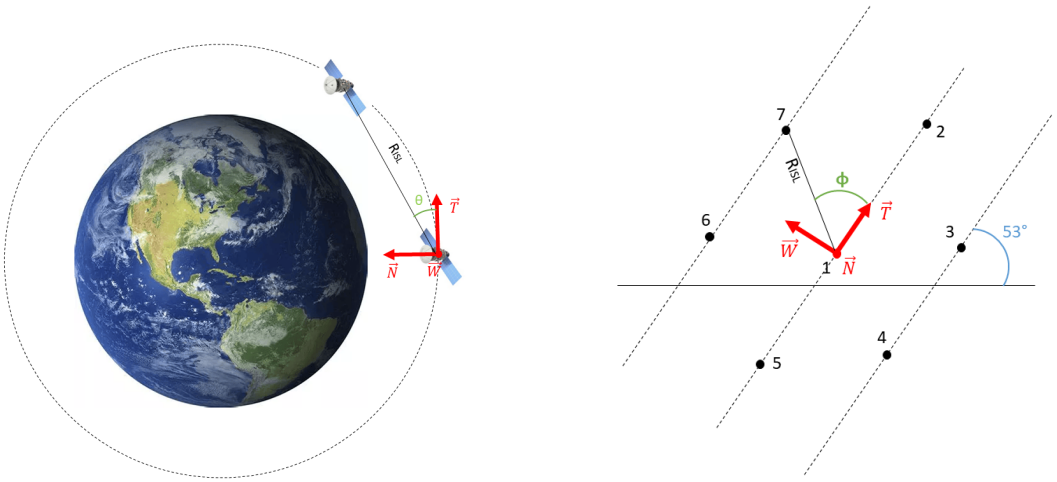

Figure 4.7: 2D representations of elevation θ (left) and azimuth ϕ (right) angles (dimensions are not proportionate).

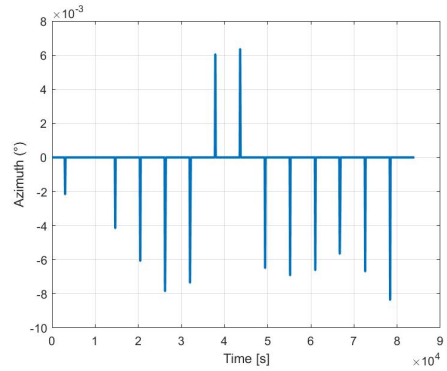

(a) Slave satellite 2.

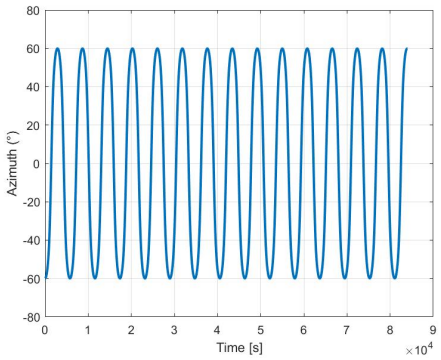

(b) Slave satellite 3.

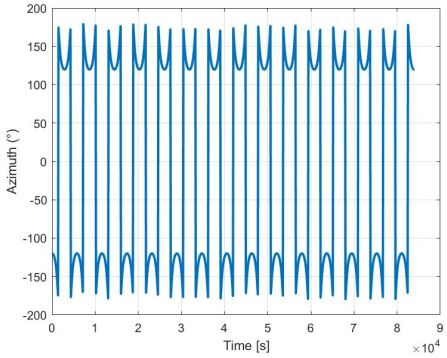

(c) Slave satellite 4.

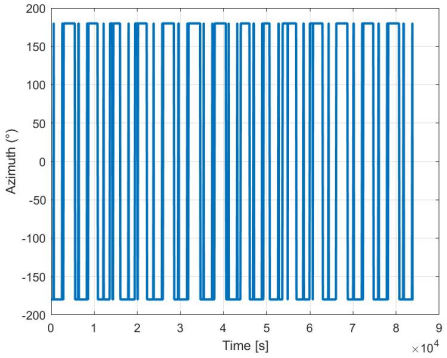

(d) Slave satellite 5.

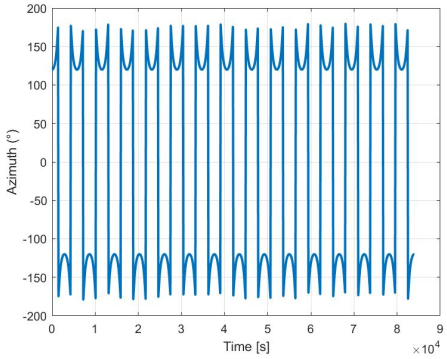

(e) Slave satellite 6.

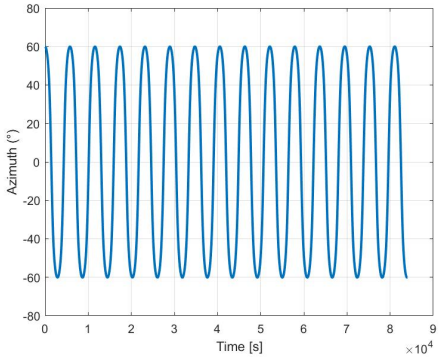

(f) Slave satellite 7.

Figure 4.8: Azimuth angle for all slave satellites at 50 m distance.

period. When the satellite has completed one orbit, the angle configuration returns to the initial one, hence a oscillation period corresponds to one orbit. Finally, the discontinuity presented in Fig. 4.9c, 4.9d and 4.9e occurs when the slave satellite crosses the orbit behind the master, and consequently the azimuth switches between $-180°$ and $180°$. Finally, it should be remarked that orbit perturbations play a minor role slightly changing the azimuth values from the theoretical ones. Tab. 4.2 sums up the value ranges for each slave satellite at 50 m distance.

Satellite	**Azimuth range**
2	$[-0.005°, 0.004°]$
3	$[-59.998°, 59.973°]$
4	$[-119.946°, -180.000°] \wedge [119.821°, 180.000°]$
5	$[-180.000°, 180.000°]$
6	$[-120.029°, -180.000°] \wedge [120.004°, 180.000°]$
7	$[-60.179°, 60.054°]$

Table 4.2: Azimuth angle range for all the slave satellites at 50m distance.

Elevation

Fig. 4.9 shows elevation angles for all the slave satellites considering a distance of 50 m between the satellites at the equator. It should be remarked that these values represent the elevation error with respect to the simple model implemented in the MATLAB code. Although the orbits are closed to each other, a drift in the elevation direction arise due to perturbation such as solar radiation pressure and atmospheric drag. Therefore, the values will change with the distance between the orbits: the more the distance increases, the more the perturbations are intense. The resulted value ranges are summed up in Tab. 4.3.

Satellite	**Elevation range**
2	$[-0.076°, 0.076°]$
3	$[-0.042°, 0.046°]$
4	$[-0.125°, 0.127°]$
5	$[-0.076°, 0.077°]$
6	$[-0.046°, 0.042°]$
7	$[-0.127°, 0.125°]$

Table 4.3: Elevation angle range for all the slave satellites at 50 m distance.

It can be noticed that satellites diametrically opposed present equal range values but different sign for a matter of convention.

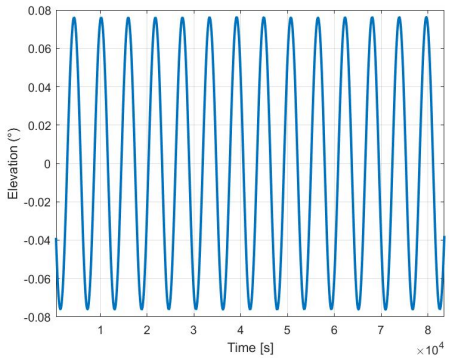

(a) Slave satellite 2.

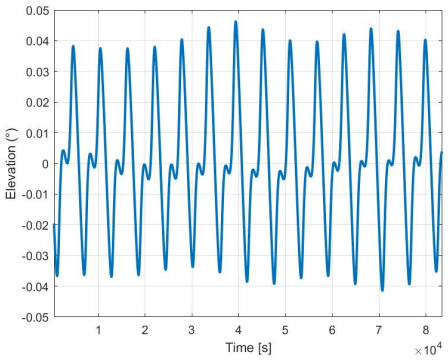

(b) Slave satellite 3.

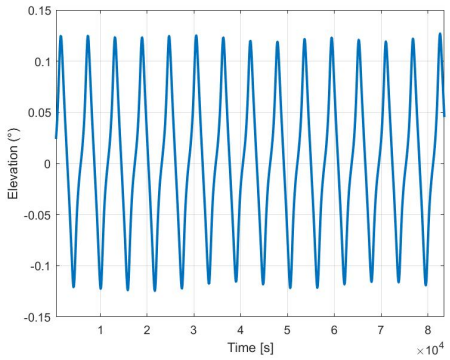

(c) Slave satellite 4.

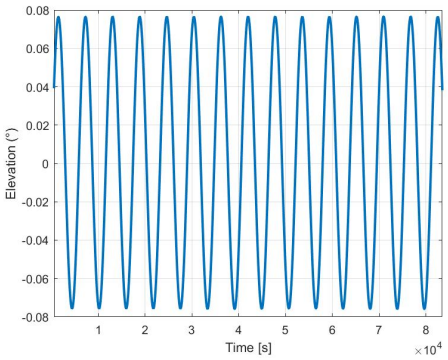

(d) Slave satellite 5.

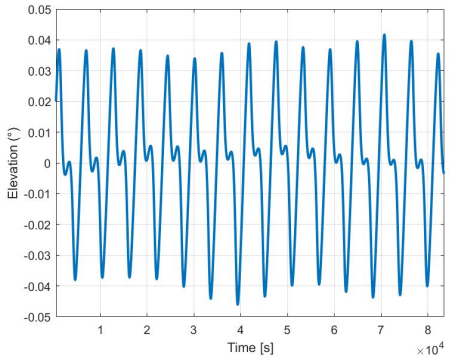

(e) Slave satellite 6.

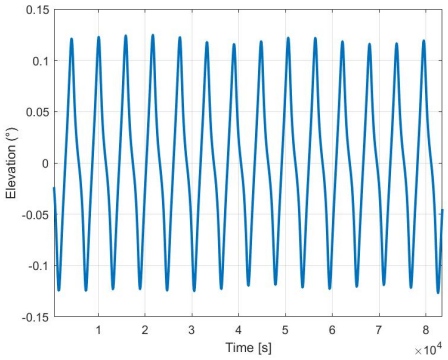

(f) Slave satellite 7.

Figure 4.9: Elevation angle for all slave satellites at 50m distance.

Furthermore, it can be seen that changing the distance between satellites (hence 100 m and 200 m), azimuth and elevation errors slightly vary (differences appear at thousandth of a degree) since the orbits stay closes to each other. In other words, the perturbation shift is almost nonexistent and can be neglected in a early design phase.

4.1.3 Pointing errors

At this stage azimuth and elevation pointing errors has to be assessed in order to determine the WPT efficiency. According to Sec. 2.2.9 a value of 0.1° can be taken into account to cover attitude instabilities. Note that it has to be summed to both azimuth and elevation errors. Regarding the orbital ones, the worst case scenario shall be identified. In other words the efficiency study shall be perform on the slave satellite linked with the highest combination value of azimuth and elevation errors. Nevertheless, the azimuth pointing shift is not straightforward to evaluate since it is influenced by interpolation and numerical errors. A value of 0.1° is taken into account for the following design. From Tab. 4.3 it can be concluded that satellite 4 represents the worst case scenario presenting pointing error of 0.127° in the elevation direction. Tab. 4.4 sums up the worst case scenario data.

Error	Value
Azimuth	0.1°
Elevation	0.127°
Attitude	0.1°

Table 4.4: Worst case scenario represented by slave satellite 4.

WPT efficiency determination

Based on Sec. 3.4 some observations relying on the LEO-Telecom mission's antenna should be pointed out. In particular, the direction corresponding to the highest dimension, i.e. 0.5 m, is more directive, hence it feels more the influence of pointing shift. For simplicity it will be called vertical direction since the antenna during its operations is placed towards the **N** axis according to the *TNW* body reference frame. Consequently, the other direction associated to 0.05 m is the horizontal one. The considered pointing errors lead to a relative efficiency of 90.5% with respect to the FNBW efficiency, that corresponds to a total radiation efficiency of 73.8%.

4.1.4 Receiving antenna design

An high level RX antenna design is carried out in this section. The goal is to find the receiving antenna dimensions thanks to the Eq. 2.35 and considering that the first lobe is caught. Tab. 4.5 presents the envisaged parameters to substitute in the diffraction formula.

Frequency	100 GHz
Horizontal TX antenna dimension	0.05 m
Vertical TX antenna dimension	0.5 m
Transmission distances	50 m 100 m 200 m
α **(FNBW)**	1

Table 4.5: Parameters' values for receiving antenna design used in the diffraction formula (Eq. 2.35).

The RX antenna dimensions found for 50 m, 100 m and 200 m are shown Fig. 4.10 and summed up in Tab. 4.6.

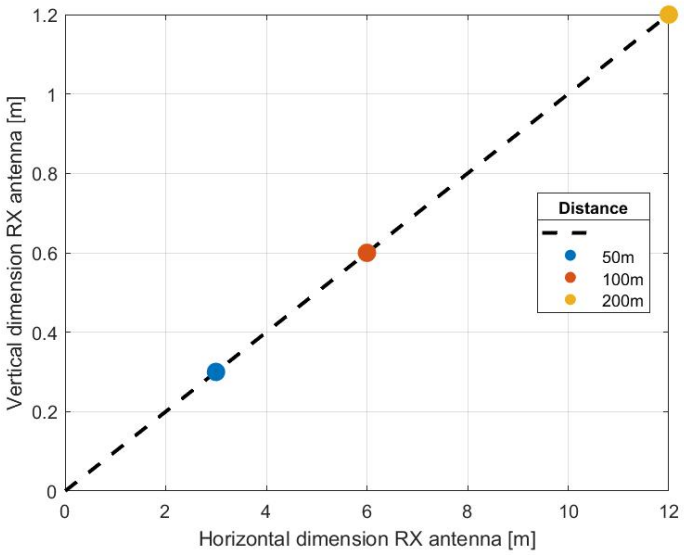

Figure 4.10: Receiving antenna dimensions varying the transmission distance at FNBW.

Note that since the diffraction formula is linear, the order of magnitude between the transmitting antenna dimensions is reflected in the receiving antenna design.

Distance [m]	Horizontal dimension [m]	Vertical dimension [m]
50	3	0.3
100	6	0.6
200	12	1.2

Table 4.6: RX antenna dimensions for 50 m, 100 m and 200 m transmission distances.

4.1.5 Transmitting antenna design

Another interesting design to perform foresees to switch point of view, fixing the receiving antenna dimensions and giving the requirements for the transmitting one as an output. To simplify, let's consider that the receiving antenna covers one face of the satellite, thus 2 m x 1 m. It is important to notice that 2 m represents what it has been called horizontal dimension, while 1m the vertical one. Therefore, TX antenna dimensions are found at FNBW always thanks to the diffraction formula, considering the same distances of transmission (Fig. 4.11). Tab. 4.7 sums up the values for the considered key distances 50 m, 100 m and 200 m.

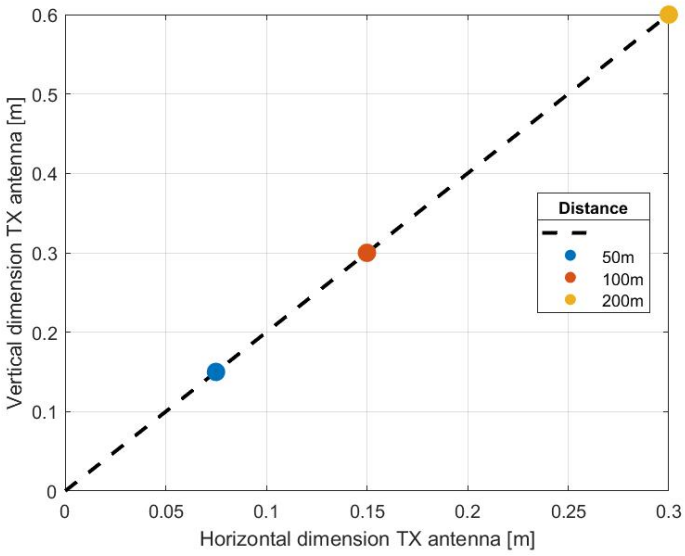

Figure 4.11: Transmitting antenna dimensions varying the transmission distance at FNBW.

Distance [m]	Horizontal dimension [m]	Vertical dimension [m]
50	0.075	0.15
100	0.15	0.3
200	0.3	0.6

Table 4.7: TX antenna dimensions for 50 m, 100 m and 200 m transmission distances.

It can be noted that with the considered size limits on the transmitting side, the

vertical dimension of 0.5 m previously taken into account is optimal for a distance of 167 m. On the other hand, the horizontal dimension of 0.05 m is optimised for 34 m distance between antennas. In other words, for a 0.05 m x 0.5 m transmitting antenna the first lobe perfectly caught at 167 m for the vertical direction and at 34 m for the horizontal one.

4.1.6 Power and mass budget

Power requirements for the non-fractionated satellite, i.e. the project above the present use case without the slave satellite concept, foresee 8500 W during daylight and 2500 W in eclipse. This leads to a 309 kg of solar array and 30 kg battery thanks to the EPS sizing formulas detailed in Sec. 2.3. The total mass is then 339 kg.
On the other hand, the fractionated system does not present power requirements since it is still in a pre-design phase and it is complicated to assess the peculiar power consuming for both master and slave satellites. Nevertheless, it is evident that SBSP concept at 100 GHz should deal with low power demands in order to present still acceptable efficiencies both in the transmission and reception chain. Slave satellites can operate exclusively on the receiving end of the communication system, significantly reducing their power consumption by leaving the task of information transmission to the master satellite. The following division is then proposed in Tab. 4.8. Although the fractionated system consumes more power

	Master	**Slave**
Daylight	7900 W	100 W
Eclipse	1900 W	100 W

Table 4.8: Power division between master and slave satellites.

due to the continuous communication between the master and slave satellites, the overall power requirements have been aligned for simplicity with those of the non-fractionated satellite, as detailed above. Therefore, the mass budget for the master is 278 kg solar array and 23 kg battery, 301 kg overall, while for each slave satellite is 5 kg and 1 kg respectively, for a total mass of 6 kg. This value shall be compared with the one derived from SBSP technology to conduct an appropriate analysis and draw accurate conclusions.
Regarding the SBSP concept, it is necessary to assess the efficiency chain in order to find the real power consumed. As shown in the previous chapter, the power transmission efficiency is 73.8% including the pointing errors. Considering both the

transmitter and rectenna efficiencies at 80%[1], the overall efficiency chain is about 47%. Hence, the master has to produce about 9177 W during daylight and 3177 W in eclipse to meet slave satellites' power requirements. The total mass on the master side is then 382 kg, 345 kg solar array and 38 kg of battery. Furthermore, rectennas has to be taken into account on slave spacecrafts for a total mass of 10.8 kg at 50 m distance with 2 kg/m^2 specific mass[2]. The added mass due to the SBSP concept is then 56.8 kg, i.e. subtracting 337 kg of the fractionated without SBSP scenario. It represents 70% reduction of mass on each slave, while 27% increment on the master side. Tab. 4.9 sums up the obtained results for each case.

	Master			**Slave**			
Mass	**Solar array**	**Battery**	**Total**	**Solar Array**	**Battery**	**Total**	**Overall**
Non fractionated	309 kg	30 kg	339 kg	-	-	-	339 kg
Fractionated without SBSP	278 kg	23 kg	301 kg	5 kg	1 kg	6 kg	337 kg
Fractionated with SBSP	345 kg	38 kg	383 kg	1.8 kg	-	-	393.8 kg

Table 4.9: Solar array and battery mass budget for the non-fractionated, fractionated without SBSP technology and fractionated with SBSP technology cases. The red value indicates the rectennas' mass.

At this point, it is interesting to carry out a parametric study varying slave's power requirements. As mentioned before, power supply values shall stay low in order to keep high the transmitting efficiencies. Fig. 4.12 show the total mass variation for both master and slaves function of slave's power requirements. The results indicate that as the power demand for each slave spacecraft increase, the mass reduction for the slaves using SBSP technology becomes more significant since rectennas' size and weight are fixed at 50 m distance. Conversely, the master satellite must generate more power, leading to an increase in its mass. Fig. 4.13 illustrates the same concept but from another point of view, i.e. mass gain for both the master and slave satellites changing slave's power demand.

[1]Actually, these values are overestimated for the current use case with the expectation that long-term technological improvements will eventually reach that point.

[2]This value does not account for the moving mechanism, as the rectennas are simply integrated as a stationary layer on the satellite's surface.

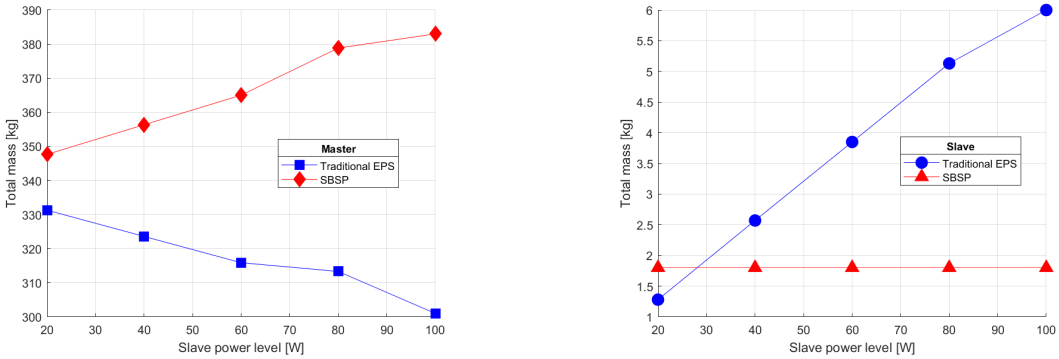

Figure 4.12: Master and slave's total mass varying slave's power demand, comparing traditional EPS design and SBSP technology.

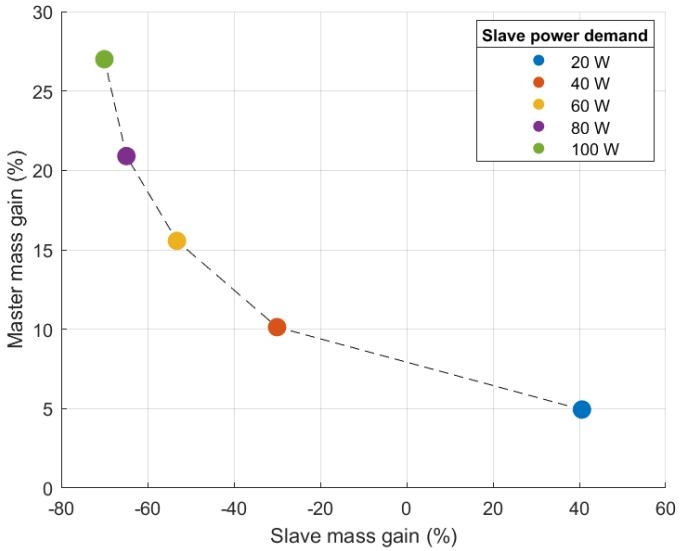

Figure 4.13: Mass gain for master and slaves varying the slave's power demand.

4.1.7 Result analysis and conclusions

The results put in evidence that the SBSP concept remains in a competitive phase when compared to traditional EPS design, particularly concerning the weight of the overall system. Size and mass of the solar arrays and batteries removed from the slave satellites are added to the master and increased due to the overall chain losses. Furthermore, power levels are limited by the transmission chain efficiency constraining the range of potential applications. Nevertheless, the advantages are remarkable on the slave satellite side. The removal of moving parts associated with the solar arrays enhances system reliability and reduce the total mass, while rectennas' layer positioned on the side facing the master's antenna simplifies the overall system design. Moreover, slave satellites benefit from a simpler and more efficient attitude and control system, as they no longer have to accommodate the bulkiness of solar arrays. Finally, the design and manufacturing process can be streamlined and expedited due to the significant reduction in the EPS components.

Chapter 5

Radio-telescope on lunar surface

Following the detection of gravitational waves, and taking into account the wealth of astronomical instrumentation across the electromagnetic spectrum, the radio frequency range below approximately 30 MHz remains the last virtually unexplored frequency domain. Earth's atmosphere reflects back all radiation from space below its ionospheric plasma frequency (around 20 MHz), and the turbulent ionosphere gives rise to "radio seeing", making ground-based radio observations of the sky more difficult at frequencies below 100 MHz but certainly prohibiting observations at the lowest frequencies.
In this context, the mission considered hereinafter, carried out by ESA, foresees to design a radio-telescope on the far side of the Moon in order to catch the radio frequency domain below 30 MHz (Fig. 5.1). The observatory aims at providing the

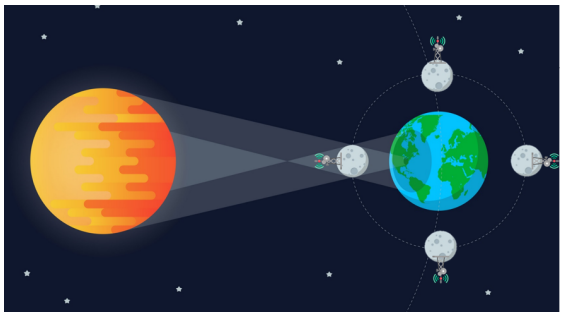

Figure 5.1: Simplified scheme of the radio-telescope project.

capability to image the entire sky extending down two orders of magnitude below bands accessible to ground-based radio astronomy. The lunar far side can simultaneously provide isolation from terrestrial radio frequency interference, auroral

kilometric radiation and plasma noise from the solar wind, representing a unique location within the inner solar system from which sky noise limited observations can be carried out at sub-MHz frequencies.

The idea to power the radio-telescope via SBSP technology comes from lunar orbit's characteristic. Because the Moon's rotation and orbital periods are tidally locked, both lasting around 28 days, each hemisphere experiences night for half of that period. Therefore, radio-telescope's batteries have to withstand around 14 days of night in a row, and consequently the mass increases exponentially. A preliminary design shows that using Li-ion technology the total mass of the battery subsystem is around 1165 kg, clearly unacceptable for the lunar lander's mass constraint. For this reason, a Regenerative Fuel Cell System (RFCS) has been taken into account to reduce battery mass up to 279 kg. Although it is within acceptable mass limits, it still represents a high value for the EPS subsystem. Moreover, RFCS technology presents a TRL of 3 for this application, making it challenging to put in place in the short term.
SBSP concept fits into this context aiming to remove batteries, considerably reducing the total weight. Actually, batteries should be always envisaged to deal with non nominal operations and security reasons, but still mass gain is enormous. The radio-telescope is supplied during the 14 day of night by a station placed in the cislunar space sending RF or optical waves to the user. Orbit and frequency selection are essential for the antennas design and considerations are carried out in the following sections.

5.1 Orbit analysis

There are some attractive types of orbit available around the Moon: halo orbit and Low Lunar Orbit (LLO). Both are detailed hereinafter showing advantages and drawbacks regarding this use case.

5.1.1 Halo orbit

Halo orbit definition and structure is explained in Appx. C. For the radio-telescope use case, the considered halo orbit is associated with L_2 Lagrange point in the three-body problem Moon, Earth and satellite. In this way, the spacecraft is always in visibility with the Earth and the far side of the Moon at the same time. Therefore, a data relay communication can be established. The first example is represented by the Chinese mission Chang'e 4 whose spacecraft landed in the Von Kármán crater on the far side of the Moon using the Queqiao relay satellite to communicate with the Earth [17].
Nevertheless Earth visibility plays a second role in the SBSP station high-level

design. The main focus relies on distance minimisation between station and user with the objective to lower antennas dimensions. From this point of view, halo orbits are far from performing, presenting high transmission distances. Just think that for Queqiao relay satellite the longest distance to the Moon is 79000 km, and the shortest one is 47000 km.
An interesting pool of halo orbits is represented by near-rectilinear halo orbit (NRHO), where most cislunar missions will happen. Its characteristic relies on the distance with the Moon's surface that varies significantly during the orbit. Usually, the perilune is few thousands of kilometres while the apolune is one order of magnitude bigger. Moreover, it is necessary to check if visibility between user and SBSP station is present at closer distances.

Communications relay orbiter

The mission shall foresee a communication relay system to exchange data with the Earth ground stations. Among all the possible communication relay spacecrafts taken into account in the pre-design phase of the radio-telescope, Lunar Orbiter Platform-Gateway (LOP-G) has been chosen for this purpose. The LOP-G will perform crewed and uncrewed Lunar Surface Operations and it will be orbiting around the Moon in a southern NRHO towards Earth-Moon L_2 libration point. It is also expected to perform orbits transfer as needed to support Moon Surface missions and possible Mars excursions. The orbit can be approximated by the following parameters summed up in Tab. 5.1. Additionally, the orbit is considered elliptical, assuming orbital maintenance manoeuvres.

Semi-major axis	35681 km
Eccentricity	0.8392
Inclination	90°
Selenographic longitude of ascending node	270°
Argument of periselenium	90°
True anomaly	180° at epoch 01/01/2025

Table 5.1: LOP-G obital parameters.

The LOP-G is expected to be constituted by different elements (see Fig. 5.2) that serve different functionalities. In particular, the Lunar Communication system, that will be accommodated on the ESPRIT module, will provide Lunar Communications and Earth Communication for science data relay, including ascending/descending vehicles. On the ESPRIT element it is expected the presence of a Ka band[1]

[1]It is a portion of the microwave part of the electromagnetic spectrum defined as frequencies

multibeam antenna pointed towards the +Z axis direction. The Ka band antenna will provide and guarantee a first link between the LOP-G and the Earth and a second one between the LOP-G and the Moon.

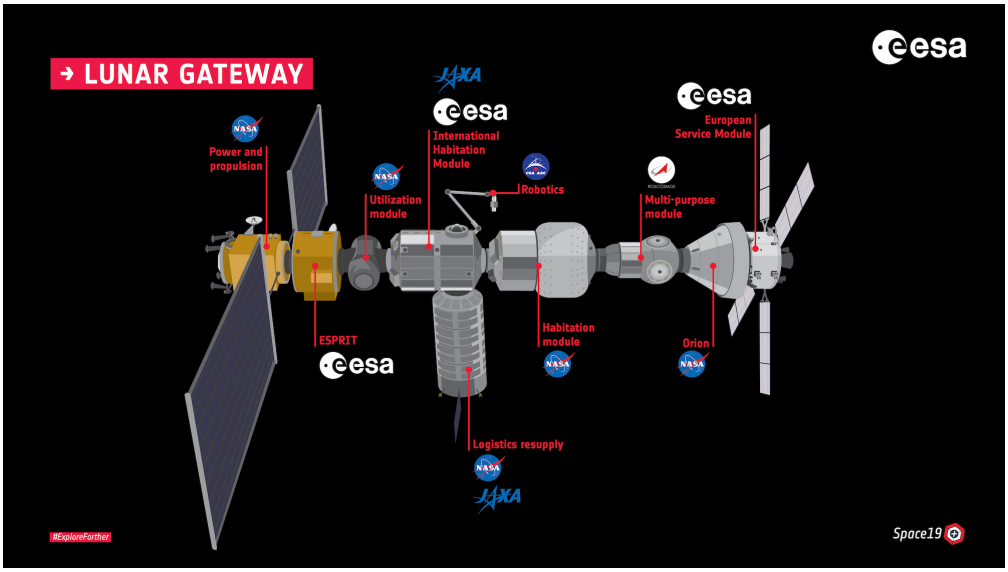

Figure 5.2: Lunar Gateway modules' organisation [18].

5.1.2 Elliptical Lunar Frozen Orbits (ELFO)

ELFO is a new class of stable altitude orbits at the Moon that satisfies required characteristics for communication relay with the Earth [19]. The orbits are elliptical with their line of apsides librating in the polar region (a.k.a. 'frozen' orbits), and exhibit lifetimes in excess of ten years, the expected mission duration for a lunar telecommunication system.

5.1.3 Low Lunar orbit (LLO)

Generally, LLO are lunar orbits below 100 km with a period of approximately two hours. Although they represent a particular interest for the Moon exploration, they suffer from gravitational perturbations that make unstable most of them. In fact, the presence of mass concentrations (called mascons) beneath the lunar surface caused by large impacting bodies at some remote time in the past has led to gravitational anomalies distorting lunar orbits. Nevertheless, there are some special

in the range 26.5–40 GHz.

frozen orbits that are not influenced by mascons, hence theirs orbital parameters are not perturbed at first order. Moreover, study of the mascons' effect on lunar spacecraft led to the discovery in 2001 of frozen orbits occurring at four orbital inclinations: 27°, 50°, 76°, and 86°, in which a spacecraft can stay in a low orbit indefinitely [20]. These would be useful for long-term stays in LLO and in particular for the radio-telescope application. Additionally, distances are way lower comparing to halo orbits bringing to a significant reduction in antennas' size. Nevertheless, communication link is not always available but there is a few minutes time slot every orbit when the user sees the SBSP station.

5.1.4 Orbit selection

Two orbits are finally selected for the power beaming application on the radio-telescope: the Lunar Gateway NHRO and the 27° inclination LLO. The former will be used only to demonstrate the WPT technology due to its higher distance from the lunar surface; the latter is selected for the final power beaming application, allowing a more feasible antenna design.

5.2 Power transmission chain's efficiency

It is important to remark that the objective of this use case study is to power the radio-telescope during 14 days of night in a row. The power requirement during the eclipse period is 300 W for a total of 100800 Wh battery capacity. It has been mentioned that this value brings to an unfeasible battery design due to an exponential growth of the mass. The SBSP concept aims to address this drawback significantly reducing the user's total mass. However, a preliminary study on the chain's efficiency must be conducted to evaluate all losses along the path.

5.2.1 Frequency selection

It has been explained that the higher is the frequency transmission, the lower is the antennas' size. Since in this use case the order of magnitude of distances between transmitting and receiving antennas is around hundreds of kilometres, the dimensions would be too large taking into account microwave frequencies. For instance, taking the LLO orbit altitude, i.e. approximately 100 km, and a 100 GHz frequency, the antennas' dimension would be 27 m using Eq. 2.35 with α equals to 2.44 for simplicity. For this reason, laser transmission is considered in the following in order to assess a more feasible design.

Laser transmission

Significant progress has been made in the development of high power, high efficiency laser diodes. Extensive studies and technological advancements have resulted in laser diodes that generate high efficiency trying to maintain high power output. Among others, the DARPA Super High Efficiency Diode Sources (SHEDS) program's goal is to design a 80% power conversion efficiency laser diode [21]. Another study demonstrates that 20-junction vertical cavity surface emitting laser (VCSEL) can achieve an electro-optical conversion efficiency of more than 88% at room temperature [22]. Although this efficiency levels allows to increase WPT performances, power output peak achieves only few dozen of Watt, definitely not enough for our client's requirements.
In the following study, a visible wavelength of 850 nm is taken into account since it corresponds to the monochromatic illumination peak response of the existing GaAs solar cells, commonly used in space applications. High efficiency GaAs cells can produce over 50% efficiency under 850 nm monochromatic laser illumination.

5.2.2 Efficiency chain

Based on what has been detailed up to here, Tab. 5.2 lists the efficiencies taken into account for the radio-telescope use case. It is important to remark that the 84%

Power conversion efficiency laser diode	80%
Power transmission efficiency (FNBW)	84%
GaAs solar cells efficiency (850 nm)	50%

Table 5.2: Laser WPT efficiencies.

power transmission efficiency comes from the integral of the parabolic reflector's radiation pattern at FNBW. It is straightforward to calculate the total efficiency, that is 34%. Nevertheless, the values are overestimated for the current use case with the expectation that long-term technological improvements will eventually reach that point.

5.3 Results

First, the study is focused on the SBSP demonstrator placed on the Lunar Gateway, thus in NHRO. The objective is to assess the power beaming technology with the radio-telescope on the lunar surface. Then, the design shifts to the SBSP station on the LLO orbit where the transmission distances are reduced, hence more attractive for a feasible WPT application.

The orbit simulations are run on GMAT software using the predefined lunar gravity model *LP-165*. Based on data from lunar missions, it offers coefficients that describe the Moon's gravitational potential field up to degree and order 165. This high value allow for detailed representation of the Moon's gravitational anomalies. In addition, the considered perturbations include the influences of the Sun and Earth, as well as solar radiation pressure.
The goal of the simulations is to determine the visibility between SBSP station and radio-telescope on ground during the 14 Earth days of night (half of a lunar day), key input for the power beaming pre-design. It should be noticed that the simulation starting date has minimal impact on the results, making it a less critical parameter for the studies hereinafter.
In the following simulations, it should be pointed out that the chosen reference frame is body fixed, hence it rotates with the Moon. The radio-telescope ground coordinates refers to the Tsiolkovsky crater, selected as baseline for its pre-design phase study. The latitude is $-22°$ *S*, while the longitude varies during the simulation, going from dusk to the following dawn. Remember that Moon's axis rotation and ecliptic plane form an angle of about 5°.
Regarding the communication link, the minimum elevation angle for initiating data transmission is 5°. Therefore, the total ground visibility angle is 170°.
Tab. 5.3 sums up some Moon's gravitational and geometrical properties, useful for the following calculation.

Standard gravitational parameter	$4.9 \cdot 10^{12} \frac{m^3}{s^2}$
Average radius	1737 km

Table 5.3: Moon's gravitational and geometrical properties.

5.3.1 NHRO power beaming demonstrator

The Lunar Gateway NHRO orbit's characteristics are shown in Sec. 5.1.1. From the fundamental formulas of Keplerian orbits detailed in Appx. B it is straightforward to calculate the perilune and the apolune, respectively 5738 km and 65625 km. Form Eq. B.3 the orbital period is about 7 terrestrial days, while the velocity at the perilune is 1.25 km/s thanks to Eq. B.2.
The simulation has been run on GMAT for six Earth month from the 1st January 2025. Fig. 5.3 shows the chosen NHRO orbit with respect to the body reference frame that rotates with the Moon.

Fig. 5.4 displays respectively altitude, velocity magnitude and RAAN variations over the orbit. It should be remarked that the RAAN variation is calculated with respect to the body reference frame that follows Moon's rotation. Notice that the values previously found with the basic keplerian formulas are verified.

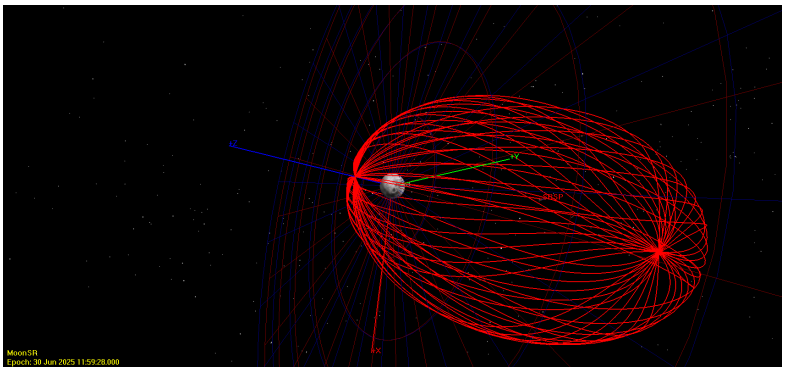

Figure 5.3: Considered NHRO orbit on 6 month GMAT simulation wrt body reference frame.

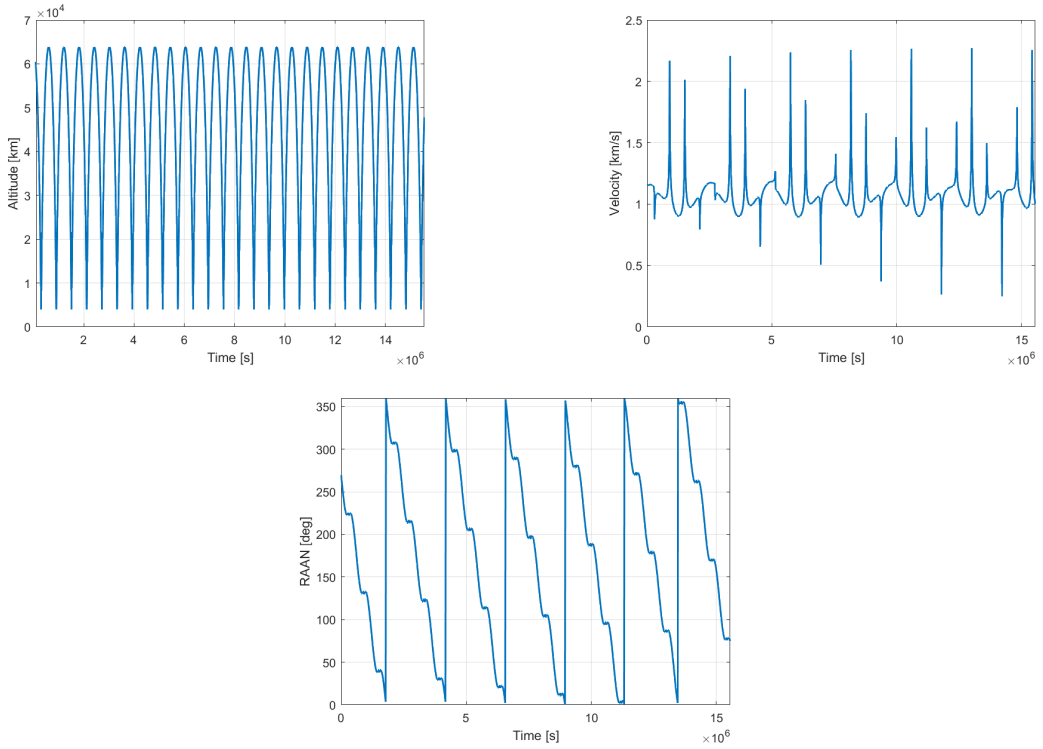

Figure 5.4: Altitude, velocity and RAAN variations during the simulation.

The ground track (Fig. 5.5) is useful to assess the communication link between the SBSP demonstrator and the radio-telescope on ground. Tab. 5.4 lists all the available time slots with the respective duration during the 6 month simulation. It should be noted that visibility periods are separated by non-visibility intervals lasting between 1 and 2 days. Moreover, since the orbit is elliptical, the spacecraft passes most of the time near the apolune, where distances between the lunar surface are higher.

Starting date	**Closing date**	**Duration [day]**
01 Jan 2025 11:59:28	03 Jan 2025 05:50:07	1,7
05 Jan 2025 01:29:34	11 Jan 2025 22:40:20	6,9
13 Jan 2025 19:02:08	18 Jan 2025 22:31:51	5,1
19 Jan 2025 23:44:34	24 Jan 2025 17:53:36	4,8
26 Jan 2025 01:23:53	31 Jan 2025 08:47:57	5,3
02 Feb 2025 01:57:19	08 Feb 2025 22:59:05	6,9
10 Feb 2025 20:16:07	15 Feb 2025 22:21:17	5,1
16 Feb 2025 19:13:51	21 Feb 2025 14:11:17	4,8
23 Feb 2025 01:26:38	28 Feb 2025 13:36:06	5,5
02 Mar 2025 02:37:39	08 Mar 2025 23:14:34	6,9
10 Mar 2025 20:42:02	15 Mar 2025 21:57:54	5,1
16 Mar 2025 14:46:07	21 Mar 2025 11:01:37	4,8
23 Mar 2025 01:31:53	28 Mar 2025 21:15:17	5,8
30 Mar 2025 03:44:38	05 Apr 2025 23:27:45	6,8
07 Apr 2025 20:27:16	12 Apr 2025 21:10:56	5,0
13 Apr 2025 10:43:42	18 Apr 2025 08:27:09	4,9
20 Apr 2025 01:39:04	26 Apr 2025 07:54:58	6,3
27 Apr 2025 05:56:16	03 May 2025 23:39:10	6,7
05 May 2025 19:35:35	10 May 2025 19:42:22	5,0
11 May 2025 07:30:53	16 May 2025 06:29:00	5,0
18 May 2025 01:47:51	21 May 2025 11:59:27	3,4

Table 5.4: Starting and closing date for the communication link between SBSP demonstrator and user on ground during the 6 month simulation.

Parabolic laser reflector dimensions

First, it is necessary to determine the solar array dimensions, knowing that the required power for operations is 300 W. Considering a radio-telescope lifetime of 10 years and a solar array efficiency of 40%, the area is approximately 0.72 m^2, corresponding to a diameter of 0.96 m. As previously mentioned, the diffraction

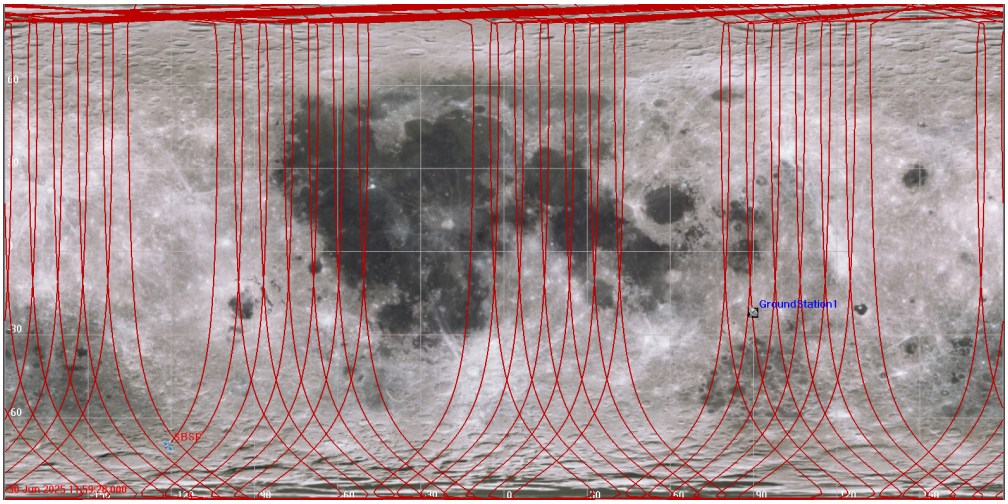

Figure 5.5: SBSP spacecraft ground track, where 0° longitude refers to the opposite point to the Sun line.

formula (Eq. 2.35) is also valid in the visible domain of the electromagnetic spectrum. Given a transmitting wavelength of 850 nm and an average distance around the perilune of 6000 km, the laser reflector diameter is around 5.5 m at HNBW. The obtained value is clearly unfeasible, mainly for a matter of costs[2]. For this reason, a receiving reflector is envisaged to increase the effective receiving area, thereby allowing a reduction in the size of the transmitting laser reflector. This receiving reflector could be made of aluminium, which is significantly less expensive than the transmitting lens. A limit of 1 m is set for the reflector diameter at the transmission in order to contain the cost spread and the calculation is redone. Fig. 5.6 show the parametric study taking into account the envisaged limits. It

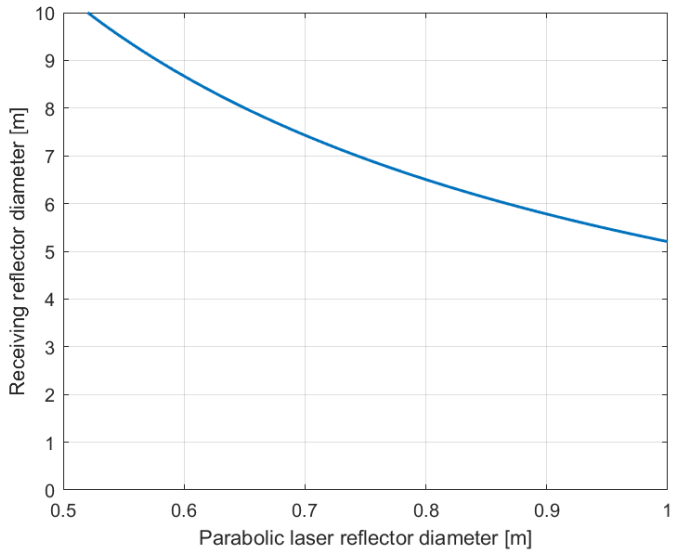

Figure 5.6: Transmitting and receiving parametric study setting 1 m and 10 m limit respectively for lens and receiving reflector diameter.

should be remarked that the objective of this WPT demonstrator is to assess the technology and the power beaming concept; hence, performances play a minor role. For these reasons, the transmission system design is performed at closer distances and at HNBW in order to reduce the dimensions.

5.3.2 LLO SBSP station

Now, the SBSP station is placed at 27° inclination LLO, 100 km of altitude and 0° RAAN with respect to the inertial reference frame. The inclination value has been

[2]Notice that the 2.4 m diameter Hubble Space Telescope's mirror costed several million dollars.

chosen among the others to maximise the visibility time between SBSP spacecraft and user. The ground station's visibility is geometrically defined within a 40° cone, with its vertex at the Moon's centre. Consequently, the latitude visibility range spans from −42° to −2°, given that the radio telescope is positioned at −22°. Generally, the stability of this orbit, coupled with its proximity to the user, makes it appealing for power beaming applications. The orbital mechanics formulas presented in Appx. B permits to determine the orbital period and velocity of the spacecraft. The eclipse period is geometrically determined (see Fig. 5.7) and it will be relevant for the EPS sizing. Fig. 5.8 shows visibility between SBSP station and user taking into account 5° minimum elevation angle to set the communication link.

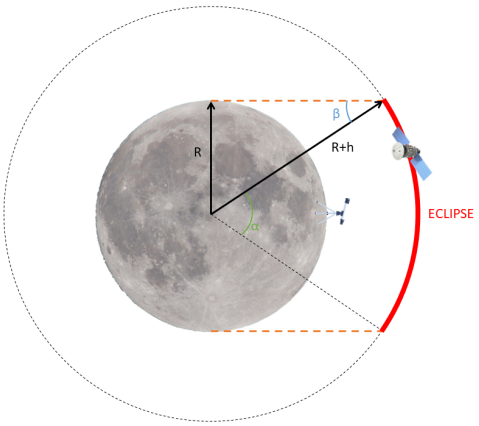

Figure 5.7: Eclipse period calculation for circular orbit.

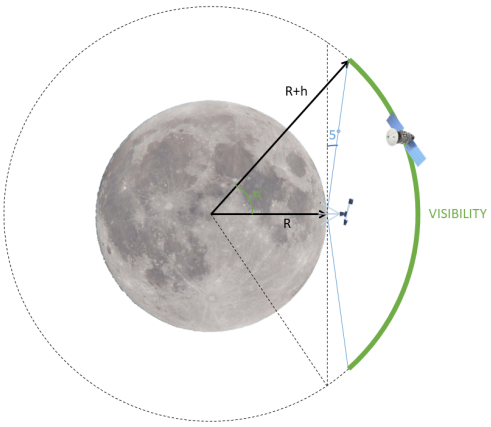

Figure 5.8: Geometric scheme to determine the visibility period between the radio-telescope and SBSP orbiter.

The chosen orbital parameters and properties are summed up in Tab. 5.5.

Altitude	100 km
RAAN	0°
Period	1.96 h
Velocity	1.63 km/s
Eclipse period	39.4%
Obits in 14d	171

Table 5.5: Orbital parameters and properties of the chosen LLO.

The simulation has been run for 14 Earth days. Fig. 5.9 shows respectively altitude, velocity and RAAN variations over the orbit due to the perturbations taken into account (SRP, Earth and Sun point masses, Moon's gravitational model). Remember that the RAAN is measured relative to the body-fixed reference frame, which explains the significant variation observed during the simulation. To calculate the total shift in RAAN, it's important to note that the fixed reference frame rotates by 180° over half a day. Thus, at the end of the simulation, subtracting this rotation reveals the delta RAAN with respect to an inertial reference frame, resulting in a final shift of approximately 20°.

The ground track on the lunar surface is shown in Fig. 5.10. The ground station is initially placed at 90° longitude, representing the dawn at the beginning of the simulation with respect to a non inertial reference frame that moves with the Sun. It can be noticed that with this particular choice of parameters, the orbit inclination increases the density of ground tracks near the user, thereby extending visibility duration.

Fig. 5.11 displays the visibility time slots occurred during the simulation taking into account the 5° minimum elevation angle to establish data transmission. The sum of all of them gives a total duration of 18.23h.

Nevertheless, it is pivotal to identify the worst case scenario to proceed with the design, and this situation is not clearly the case. If the ground station shifts its longitudinal position to −40°, corresponding to the region not covered by the orbit during the simulation, the overall visibility period is reduced to just a few minutes. This is the reason why it is necessary to envisaged more satellites in order to increase the total visibility, consequently reducing the power delivered to the ground user.

Two SBSP stations

First, another SBSP spacecraft is placed on the same orbit but with opposite RAAN, hence 180°. The objective is to cover the gaps left by the first SBSP orbit in order to obtain a sufficient visibility value for the whole simulation. Fig. 5.12

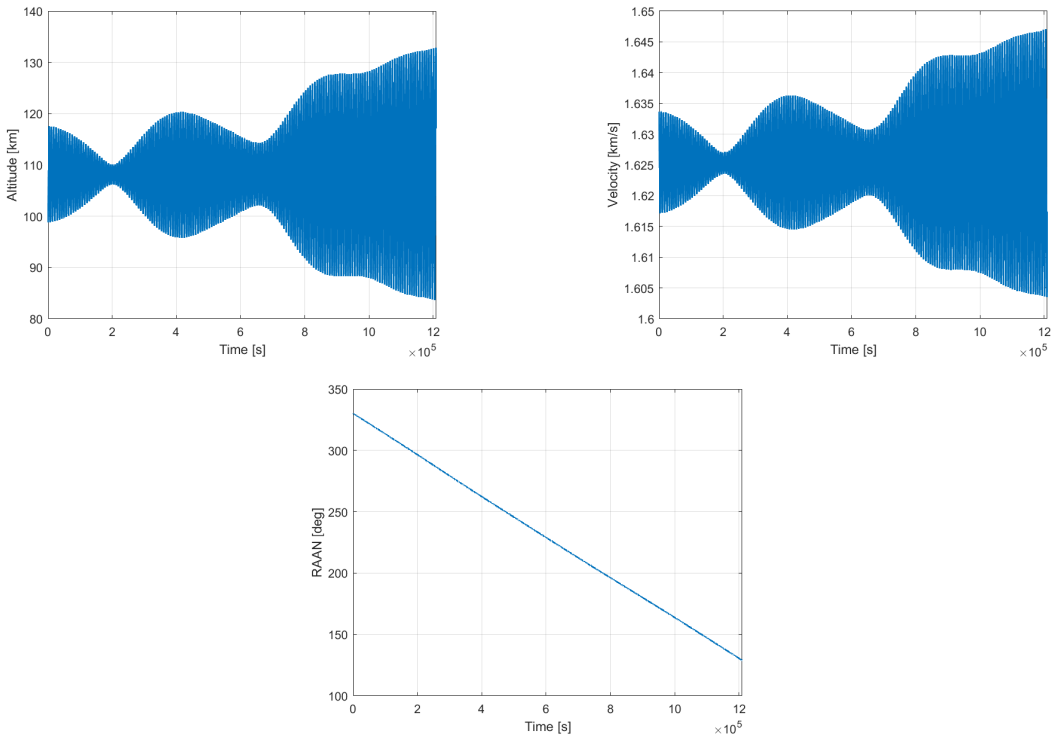

Figure 5.9: Altitude, velocity and RAAN variations during the simulation.

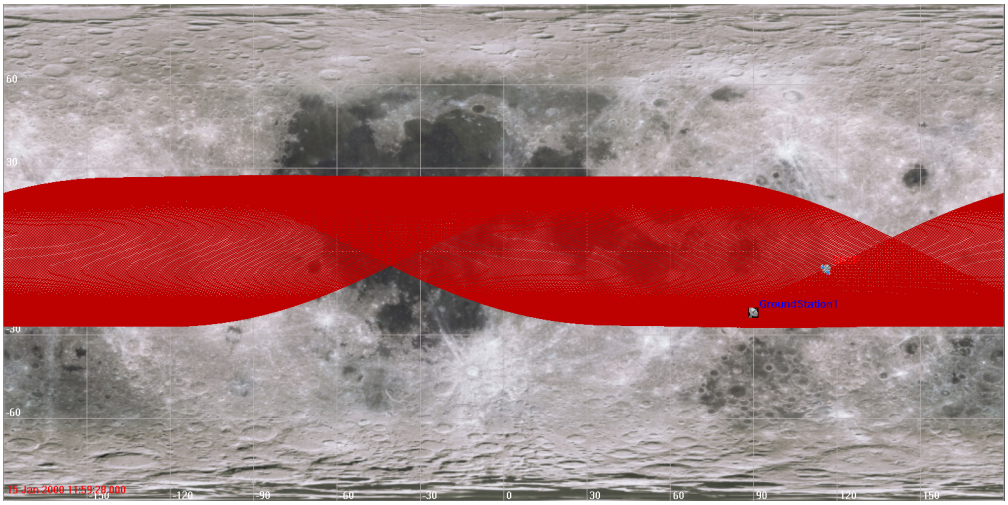

Figure 5.10: SBSP spacecraft ground track, where 0° longitude refers to the opposite point to the Sun line.

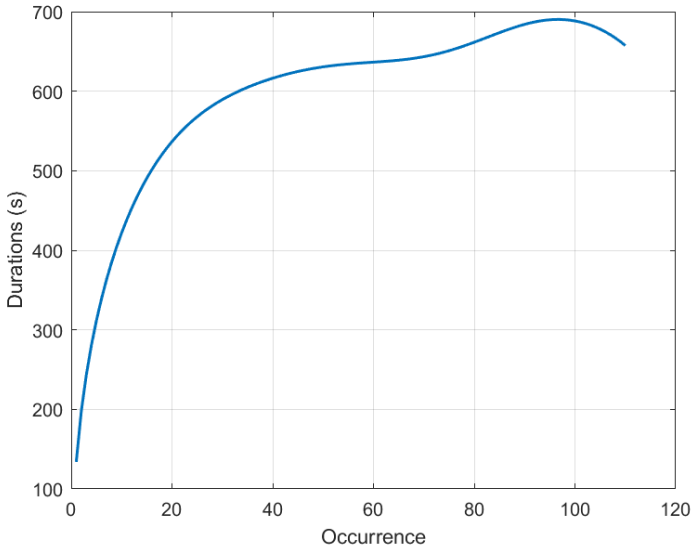

Figure 5.11: Visibility time slots occurred during the simulation.

shows the SBSP stations' ground tracks: here, the ground station placed at $-40°$ longitude is well covered by the added SBSP station.

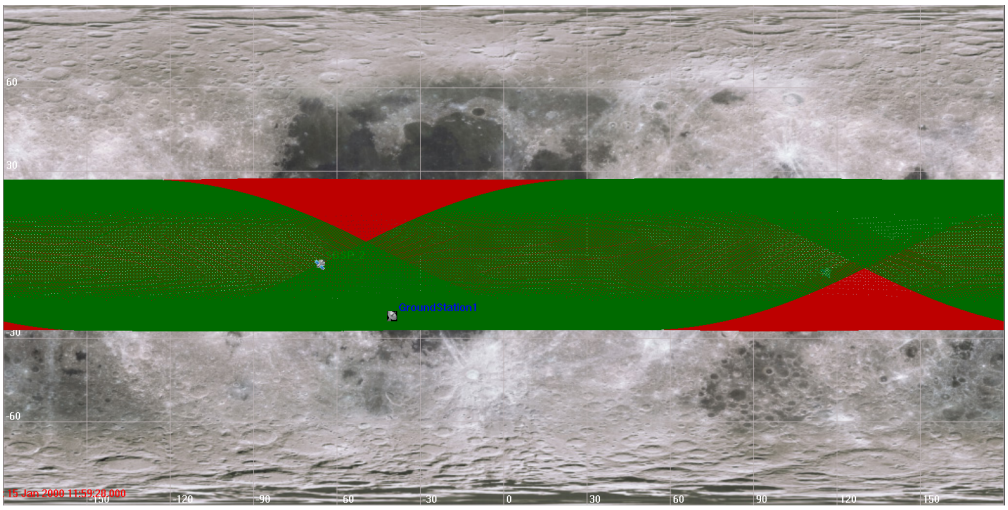

Figure 5.12: Ground tracks of the two SBSP spacecrafts, where 0° longitude refers to the opposite point to the Sun line.

The total visibility time passes from a few minutes to 19.24h, hugely improving the design. Visibility time slots are displayed in Fig. 5.13.

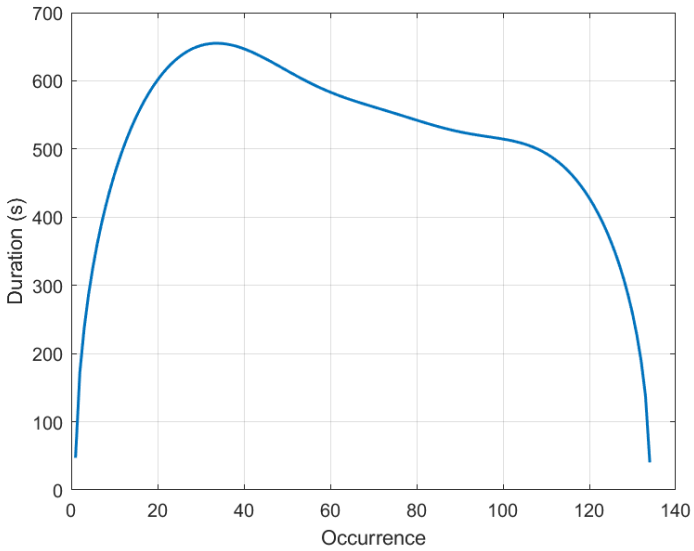

Figure 5.13: Visibility time slots occurred during the simulation.

This represents the worst case scenario, hence the starting point to carry out

the design. Nevertheless, for the ground battery design the visibility duration distribution during the simulation shall be taking into account. In this case, Fig. 5.14 shows that the user cannot see the SBSP stations for more than two days in a row at the end of simulation, dramatically increasing the ground battery capacity, and consequently its weight.

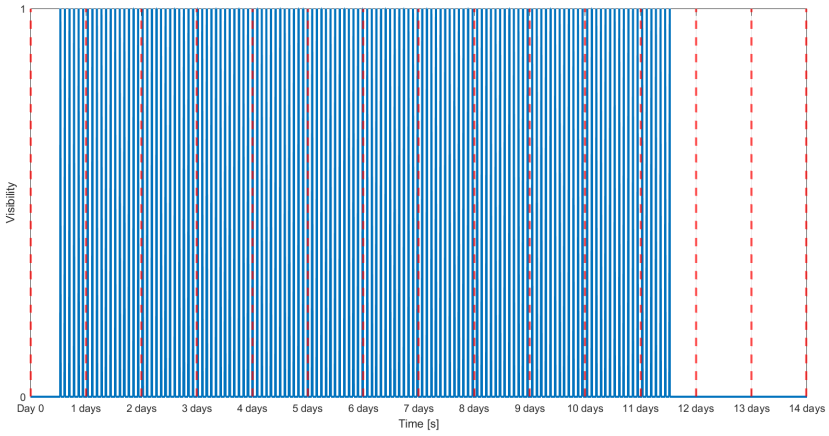

Figure 5.14: Visibility slots during the simulation: 1 means visibility, 0 otherwise.

Fig. 5.15 displays the battery cycle during the 14-day simulation. Notice that a capacity below zero leads to a bug in the design since the energy budget is losing, and the battery requires more power. Therefore, the initial demand shall be compensated storing energy from the solar arrays during the daylight[3]. Calculations have been carried out supposing that the SBSP station always delivers the same amount of power during the visibility duration. Knowing that the energy consumed by the radio-telescope in the 14 days of night is 100800 Wh and assuming a power link always active during the available time slots, the power received is:

$$\frac{100800\,Wh}{19.24\,h} = 5239\,W$$

Most importantly, the 20000 Wh capacity peak value results in a battery mass of approximately 156 kg taking into account classic values of 150 Wh/kg and 0.95 respectively for battery specific capacity and transmission line efficiency. The considered battery DoD is set at 90% since it should withstand only 27

[3]The minimum capacity value, i.e. about -5000 Wh, shall be foreseen in the solar array sizing to identify its dimensions.

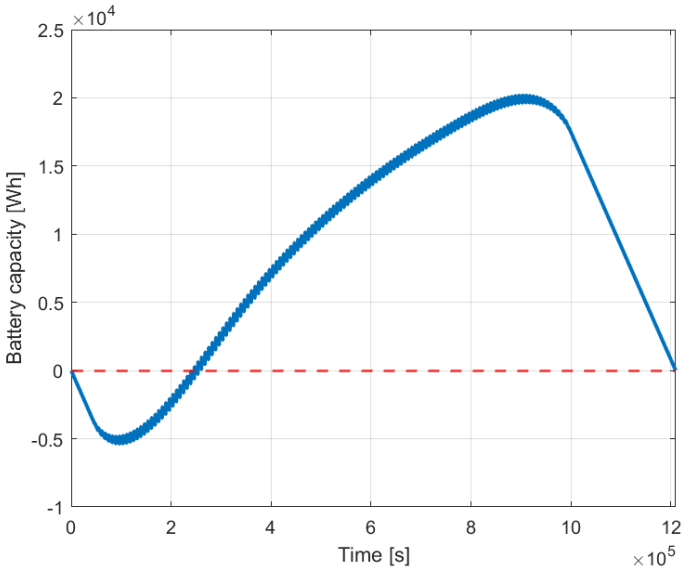

Figure 5.15: Battery capacity cycle during the 14-day simulation.

cycles per terrestrial year[4]. Since this is due to the extended periods of non-visibility, respectively at the beginning and at the end of the simulation, strategically introducing an additional spacecraft will significantly reduce the battery weight on ground.

Three SBSP stations

Hereinafter, three SBSP spacecraft are placed in 100 km orbits, 27° inclined, equally RAAN shifted over 360°. In this way, visibility with the user is more continuous during the 14 days, consequently reducing the battery mass on ground. Nevertheless, adding another spacecraft with all its subsystems will increase the total mass other than rising complexity. Therefore, a preliminary mass budget shall be made in order to identify which is the best option.
Fig. 5.16 shows the SBSP stations' ground tracks. Here, the ground station placed at −170° longitude represents the worst case scenario since the total visibility duration is the lowest among all the possibilities.

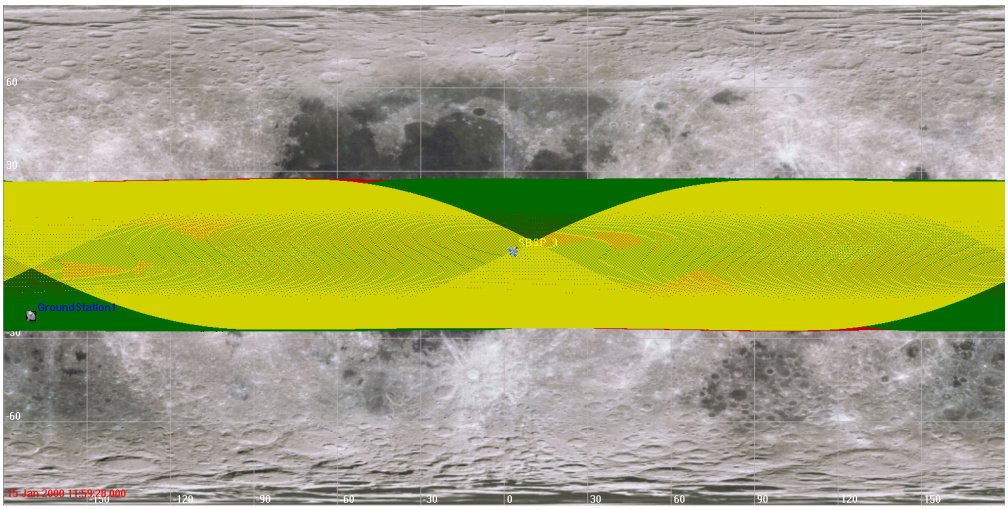

Figure 5.16: Ground tracks of the three SBSP spacecrafts, where 0° longitude refers to the opposite point to the Sun line.

Fig. 5.17 displays first and second SBSP station' visibility duration; the total period is 17.2h and 14.4h respectively for 31.59h overall. The available slots compensate for each other, leading to a more efficient distribution of visibility

[4]Note that for GEO missions, where approximately 100 cycles per year are required, the battery DoD can be high as much as 75%.

throughout the simulation period. Fig. 5.18 remarks this observation, displaying the distribution type and intersection over the 14-day time frame.

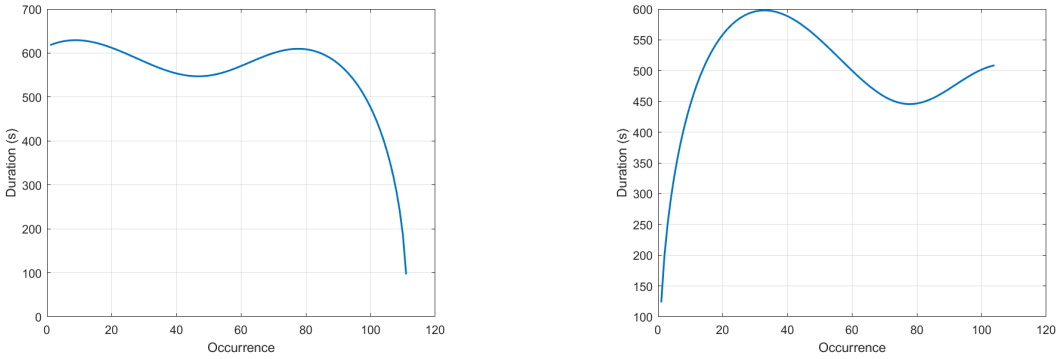

Figure 5.17: Visibility time slots occurred during the simulation for satellite 1 and 2. The visibility duration of the third SBSP station (yellow ground track) is negligible.

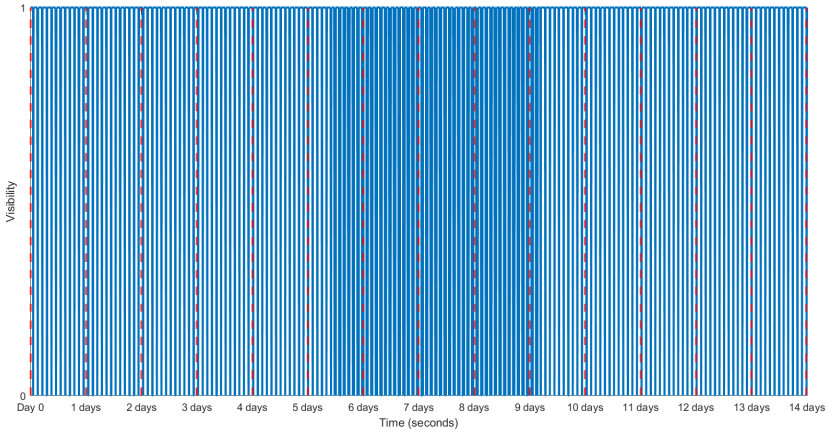

Figure 5.18: Visibility slots during the simulation: 1 means visibility, 0 otherwise.

Hereinafter, the total system mass budget is carried out; the final goal is to compare this value in the different scenarios and choose what is the best solution. The power received by the radio-telescope on ground is calculated from the different visibility duration of the two satellites. In other words, the total energy required during the 14 days of night, i.e. 100800 Wh, is split up considering the different visibility periods.

$$1)\ 100800\,Wh\,\frac{17.2\,h}{17.2\,h+14.4\,h}=54883.2\,Wh$$

$$2)\ 100800\,Wh\,\frac{14.4\,h}{17.2\,h+14.4\,h}=45916.8\,Wh$$

Therefore, the first satellite has to deliver 54883.2 Wh of energy while the second 45916.8 Wh. The power received by the ground user is easily found dividing by the respective visibility duration, resulting in approximately 3191 W.

To calculate the amount of power produced by the SBSP spacecraft, it is necessary to take into account all the WPT efficiencies (listed in Tab. 5.2) as well as the certain pointing error. Evaluating the latter is not straightforward, hence for this analysis, the relative efficiency assumed is the same as that used in the previous use case, which is 90%. Thus, all the ingredients are give to calculate the total power produced at the transmission:

$$\frac{3191\,W}{0.5\cdot 0.84\cdot 0.9\cdot 0.8}=10512\,W$$

SBSP spacecraft battery and solar array

The value just found coincides with the power that the battery has to delivered since the SBSP station is located in eclipse when the communication is set. Battery mass is calculated from sizing formulas detailed in Sec. 2.3, in particular Eq. 2.37. The considered time shall determine the maximum capacity, i.e. the worst case scenario, and coincides with the max among all the visibility periods, thus 600 s (see Fig. 5.17). At each orbit the battery will be recharged to meet the radio-telescope's power requirements, but always with a capacity less than that one envisaged. The mass value is approximately 41 kg taking into account a DoD of 30% due to the low orbit, and a transmission efficiency between battery and load of 0.95. This has to be multiplied for all the three satellites for 123 kg overall. Note that these considerations address only the power needed for the SBSP link. To be more realistic, the power required for all other spacecraft operations should also be included in the battery sizing.
At this stage, it is interesting to determine the solar array size needed to recharge the battery in the worst case scenario, thus:

$$10512\,W\cdot\frac{600\,s}{3600\,\frac{s}{h}}=1752\,Wh$$

Knowing that orbit daylight lasts 1.176 h, the power that the solar array has to deliver is 1490 W. Considering an efficiency line of 0.85 between solar array and battery, 35% solar cell energy-conversion efficiency and 10 year lifetime, the area and mass values are respectively 4.33 m^2 and 43 kg (see Tab. 3.1 for the remaining data). It should be remarked that these values are only linked with the SBSP application, and do not contain any other power notion.

Ground station battery

Fig. 5.19 shows the total energy budget on ground over the simulation.

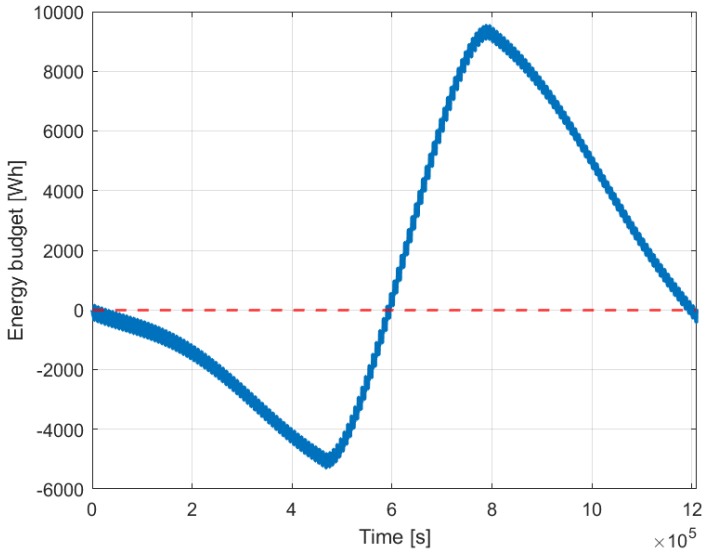

Figure 5.19: Energy budget on ground over the simulation.

It is evident that a battery is required to storage the energy. The sizing shall be done at the capacity min value, i.e. 5300 Wh. The resulting mass with a specific capacity of 150 Wh/kg, 90% DoD and 0.95 transmission line efficiency is around 42 kg. Fig. 5.20 represents battery capacity at every cycle: the presented marge with respect to zero is contained in the DoD. It should be noted that the initial value is also reached at the end, thus solar arrays have to barely recharge the battery for the next cycle, resulting in a significant mass and size reduction. Moreover, increasing the battery capacity should be envisaged, as the current limit is reached for most of the simulation time, resulting in wasted power from the SBSP station. This additional capacity would enhance safety, increasing the system reliability during operations.

To conclude, the total mass considering all the batteries is 165 kg, resulting in a 86% reduction with respect to the 1165 kg traditional Li-ion battery design.

Parabolic laser reflector dimensions

Setting 1 m limit for the parabolic laser reflector diameter as previously done in the NHRO demonstrator study, a parametric study is carried out to obtain transmitting and receiving rage sizes. Supposing 5° minimum elevation angle for initiating data transmission and 100 km distance at the nadir, it is easy to calculate the maximum

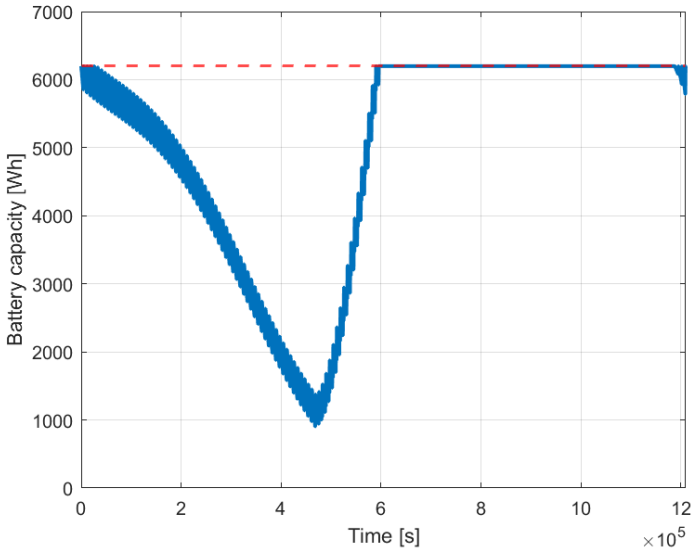

Figure 5.20: Battery capacity on ground over one cycle taking into account 90% DoD and 95% transmission line efficiency between battery and load. The red dashed line indicates the maximum battery capacity.

transmitting distance, hence when the SBSP spacecraft has just entered in the ground station visibility field. The value is 1147 km and represents the point where the dimensioning has to be performed. Setting 1 m limit lens diameter at this distance, the diffraction formula (Eq. 2.35) gives a receiving reflector size of 2.38 m. Fig. 5.21 displays the parametric study function of distance. In conclusion, the

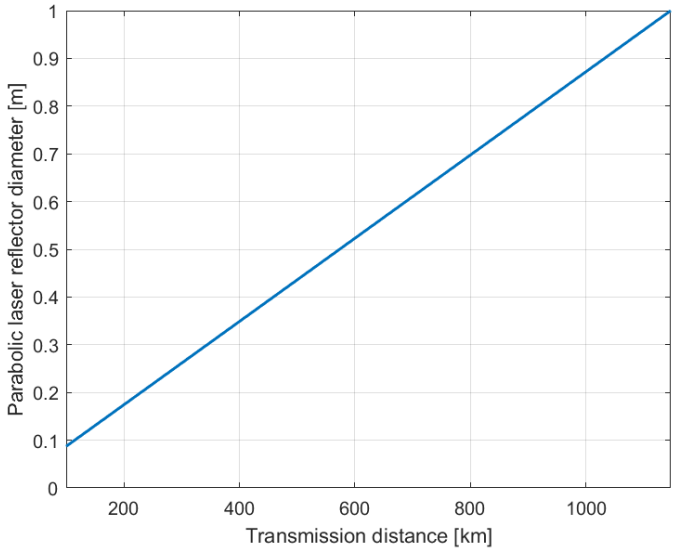

Figure 5.21: Parabolic laser reflector diameter function of the transmitting distance with 2.38 m receiving reflector size.

maximum diameter for the lens is set at 1 meter to keep costs low. Consequently, the minimum size for the receiving reflector is 2.38 meters, though increasing its size would further reduce the lens diameter and associated costs. To minimise the size of the receiving reflector, it could be considered designing the demonstrator with a lower transmission efficiency value (less than HPBW), as performance is not the primary objective.

5.3.3 Scientific mission

Generally, the LLO represents a key position for a satellite to perform scientific lunar missions. Positioned close to the lunar surface, a Low Lunar Orbit provides an optimal platform for high-resolution mapping, gravitational studies, and surface imaging. This proximity allows for the precise collection of data crucial for understanding the Moon's geological history, composition, and potential resources. Therefore, an interesting idea is to add a scientific payload to the previously designed SBSP station, significantly enhancing its value and appeal. Hereinafter,

some proposition are listed and briefly detailed.

Gravitational and magnetic field study Equipped with a gravimeter and a magnetometer, the spacecraft is able to measure the lunar gravitational and magnetic field with high accuracy. Data collected would help refine models of the Moon's internal structure, providing insights into its composition and evolution. Repeated passes over the same regions would help to detect anomalies, such as lava tubes or mascons. Moreover, the magnetic field study can provide insights into the solar wind's interaction with the lunar surface.

Surface and Subsurface Imaging The combination of high-resolution camera and Synthetic Aperture Radar (SAR) conduct to a detailed study of the lunar surface and subsurface features. High-resolution optical imagery can capture detailed surface features, including craters, ridges, and rilles[5], while SAR can penetrate the surface to reveal subsurface structures and help map areas that are permanently shadowed. This data would be valuable for selecting future landing sites and understanding geological processes.

Lunar Topography Mapping Creating a detailed topographic map of the lunar surface is pivotal to assess future landing sites. A laser altimeter can perform this task measuring the distance from the satellite to the lunar surface with high precision. This data can be used to create high-resolution digital elevation models (DEMs) of the Moon, crucial for navigation, landing site selection, and understanding lunar geomorphology.

[5]Lunar rilles are long, narrow depressions or channels on the lunar surface that resemble valleys or trenches [23].

Chapter 6

Conclusions

From the use cases detailed in the previous chapters, it is clear that SBSP technology is generally not yet ready to compete with traditional EPS. The vast distances involved significantly increase the size requirements for transmission and reception equipment, making SBSP applications impractical in most cases. Even for transmissions spanning only a few kilometres, antenna dimensions can reach several meters. Increasing transmission frequency could potentially address this issue, but it introduces complications in controlling the narrow beam, increasing pointing errors. Moreover, the reliability and efficiency of solar arrays and batteries is still far to reach. Nevertheless, specific applications could benefit from SBSP technology. Notably, the SBSP concept appears to be the best choice for scenarios involving long eclipse periods, as power beaming can eliminate the need for large and heavy batteries. The 86% mass reduction achieved in the radio-telescope use case is a prime example of this potential.
The objective of this work was to provide a systematic overview of the SBSP concept, highlighting the benefits and drawbacks of this application. The two presented use cases aimed to assess the feasibility of this technology in different scenarios. At first glance, it can be observed that SBSP technology primarily relies on one formula, the diffraction formula. The limited number of parameters involved restricts the degrees of freedom, making further improvements challenging.
In summary, with current technology readiness, the SBSP concept is suitable only for specific use cases. The radio telescope project, in particular, could pave the way for promising methods in lunar exploration. While further technological advancements may expand the range of applications, for now, widespread use of SBSP remains impractical for a robust and consistent use.

Appendix A

Earth's orbit

If you are a tired flat-earther desperately seeking to change your mind, I encourage you to keep reading. Joking apart, this appendix may be trivial but is essential to understand sun visibility variation on Earth's orbits over the year.
It is known that Earth's rotation axis is tilted by about 23.44° with respect to the ecliptic plane and it remains fixed[1] in a inertial reference frame. Hence, the way to see the Sun from the Earth changes over the orbit. In particular, equinoxes and solstices are introduced to phase Earth's orbit and consequently determine seasons in most of the countries. Spring and autumn equinoxes are the points on the orbit when Earth's rotation axis is directly perpendicular to the Sun-Earth line, while summer and winter solstices happen when the axis tilts respectively toward and away from the Sun. It should be remarked that the used season convection relies on the Northern hemisphere, thus summer occurs when it is "closer" to the Sun. The Fig. A.1 sums up all the mentioned concepts fixing the Earth, thus it is the Sun that orbits around the Earth (please flat-earthers do not misunderstand). This point of view might be unorthodox but sometimes it helps to better visualise the situation. At this point, let's debunk a myth: a Sun-synchronous orbit does not always see the Sun over the year. Even a polar one will certainly present eclipse at the equinoxes, when the Sun is hidden by the Earth due to the axial tilt. It can be easily demonstrated that the eclipse period is proportional to inclination and inversely related to altitude. Considering the fact that the SSO orbit proportionally relates inclination and altitude, one of the two factors always ends up to increase the eclipse time.

[1]Here, the long-term Earth's axis motions nutation and precession are neglected.

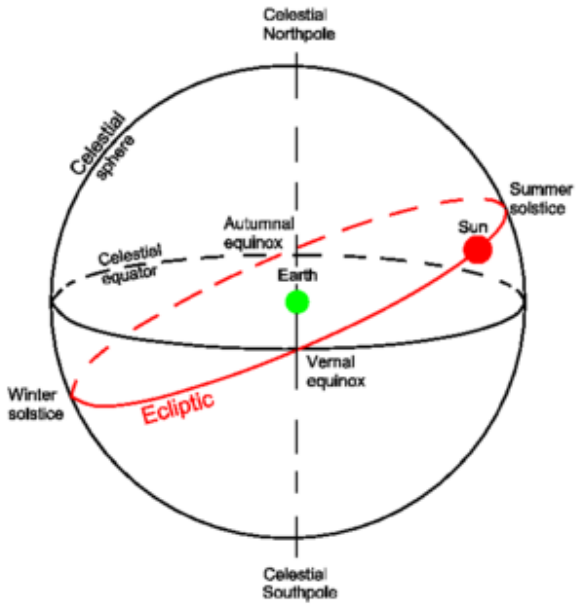

Figure A.1: Earth's orbit in a Earth fixed reference frame [24]. The red circle represents the ecliptic.

Appendix B

Basics of orbits

B.1 Orbital parameters and perturbations

Orbital elements are the required parameters to uniquely identify a specific orbit. Each of them gives the information in order to select a precise orbit among others. To help the comprehension of the following it is better to see each parameter as an additional information to get to select the chosen orbit. It should be highlight that the reference frame taken into account is the inertial one, i.e. ECI as mentioned in 2.1. Hereinafter the six traditional Keplerian[1] elements considered in a two-body system (in this case Earth and satellite) are presented:

- Semi-major Axis (a): it is the longest radius of an ellipse. It defines the size of the orbit. For circular orbits, it represents the orbit's radius.
- Eccentricity (e): it describes the shape of the orbit. It is a dimensionless parameter that ranges from 0 (a perfect circle) to 1 (a parabolic trajectory). An eccentricity between 0 and 1 indicates an elliptical orbit.
- Inclination (i): it is the angle between the orbital plane and the reference plane, i.e. the equatorial plane of the primary body. It ranges from 0° to 180° and indicates how tilted the orbit is relative to the equator.
- Longitude of the Ascending Node (Ω), mainly known as RAAN: this is the angle from the vernal equinox axis to the ascending node of the orbit, measured in the reference plane. The ascending node is the point where the orbit passes upward through the reference plane.

[1]Since the perturbations are not taken into account it is sufficient to mention Keplerian orbits for this work.

- Argument of Periapsis (ω): it is the angle from the ascending node to the orbit's point of closest approach to the primary body (periapsis), measured in the plane of the orbit.
- True Anomaly (ν): it is the angle between the periapsis and the current position of the orbiting body, measured at the primary focus of the ellipse. Nevertheless, in this work the true anomaly is substituted by an equivalent parameter, the mean anomaly (M), that has the property to progress linearly with time.

The only perturbation taken into account in this dissertation is the oblateness of the primary body (i.e. Earth) represented by the J_2 term. More in detail, the Earth is not a perfect sphere but rather an oblate spheroid, meaning it is slightly flattened at the poles and bulging at the equator. This shape can be described by higher-order terms in the gravitational potential: the J_2 term, also known as the second zonal harmonic, is the largest of these higher-order terms and should be taken into account for more precise orbit simulations. The main effects of this term are:

- RAAN precession ($\dot{\Omega}$), that is a gradual shift of the orbital plane in the equator plane. In other words the longitude of the ascending node changes over time, leading to the orbital plane rotating around the Earth's axis.
- Argument of Periapsis precession ($\dot{\omega}$), i.e. the rotation of the elliptical orbit within the orbital plane.

B.2 Keplerian orbit

This section details the fundamental formulas of Keplerian orbits. For simplicity, only the elliptical orbits are presented, as they are pertinent to this work. The specific case of circular orbits can be easily derived by setting the radius R equals to the semi-major axis a.
A elliptical orbit around a general central body can be characterised by the semi-major axis and the eccentricity e parameters. Consequently, the periastre r_p and the apoastre r_a, i.e. the closest and the furthest point to the central body respectively, are found with the following formulas:

$$\begin{aligned} r_p &= a(1-e) \\ r_a &= a(1+e) \end{aligned} \tag{B.1}$$

Then, the velocity V over the orbit is calculated from the conservation of the mechanical energy that for elliptical orbits is equal to:

$$\frac{V^2}{2} - \frac{\mu}{r} = -\frac{\mu}{2a} \tag{B.2}$$

where μ is the standard gravitational parameter and r determines the chosen point on the orbit. Another interesting parameter is the orbital period T, calculated thanks to the third Kepler's law:

$$T = 2\pi\sqrt{\frac{a^3}{\mu}} \tag{B.3}$$

Appendix C

Halo orbit

Before introducing halo orbits, it is necessary to define what the Lagrangian points represent in a three-body problem. The starting point, as a first approximation, is the Circular Restricted Three-Body Problem (CR3BP). It relies on the following notions:

- Three bodies are present (Three-Body Problem);
- One of the bodies has a negligible mass (Restricted);
- The massive bodies' orbits are circular (Circular).

This model is vastly used since it simplifies the mathematical structure of the n-body dynamical problem while still providing significant results [25]. Let's take the motion of a particle P of negligible mass that moves under the gravitational influence of two masses m_1 and m_2, referred to as the primary masses, or simply the primaries. m_1, the primary, is typically the body with the highest mass as compared to m_2, the secondary. The primaries move in circular orbits about their common centre of mass and they are not influenced by the mass of P. Assuming $m_1 \geq m_2$, the mass parameter is introduced:

$$\mu = \frac{m_2}{m_1 + m_2}$$

where $\mu \in [0, \frac{1}{2}]$ if m_2 is equal to 0 or m_1 respectively. Now, it is useful to adimensionalise variables so that the gravitational constant and the distance between the primaries m_1 and m_2 is equal to 1 and their masses are respectively 1μ and μ. Finally, the motions is considered in a rotating reference frame where the primaries are fixed in the x-axis in μ and $\mu 1$. The equations of motion obtained

are the following:

$$\begin{cases} \ddot{x} - 2\dot{y} = -\frac{\partial U}{\partial x} \\ \ddot{y} - 2\dot{x} = -\frac{\partial U}{\partial y} \\ \ddot{z} = -\frac{\partial U}{\partial z} \end{cases} \tag{C.1}$$

where U is the augmented or effective potential in the following form:

$$U(x, y) = -\frac{1}{2}(x^2 + y^2) - \frac{1-\mu}{r_1} - \frac{\mu}{r_2} - \frac{1}{2}(1-\mu)\mu$$

The equations of motion present an energy integral of motion:

$$E(x, y, z, \dot{x}, \dot{y}, \dot{z}) = \frac{1}{2}(\dot{x}^2 + \dot{y}^2 + \dot{z}^2) + U(x, y, z)$$

From now on, a reformulation of this energy integral is used, called Jacobi integral or Jacobi constant:

$$C(x, y, z, \dot{x}, \dot{y}, \dot{z}) = -2E = -(\dot{x}^2 + \dot{y}^2 + \dot{z}^2) - 2U(x, y, z) \tag{C.2}$$

The importance of this parameter is enormous since, given μ, it defines a region of possible motion for the particle P, known as Hill's region. The boundaries of this region are called zero velocity curves (zvc) and they are obtained by putting the velocity equal to zero in C.2, hence the name. Fig. C.1 shows that as the number of the Jacobi constant decreases, the forbidden areas (in pink become) less and less wide. C_i represents the maximum Jacobi constant value that allows the particle P to access the libration point L_i. The regions where the motion is possible are not connected for high values of the Jacobi constant, whereas depending on the value of the mass parameter, there is a minimum C_J for which there are no forbidden regions anymore.

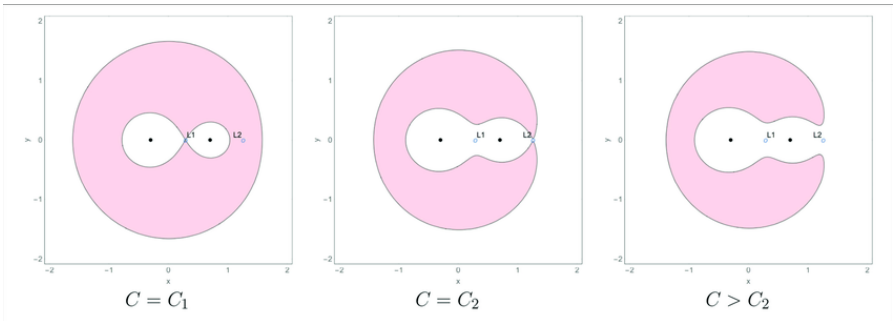

Figure C.1: Zero velocity curves for different values of the Jacobi constant [26].

Furthermore, the formulation of the equations of motion in the CR3BP implies the existence of five equilibrium points, also known as libration or Lagrangian

points. Usually designated with the notation L_i, three of them (collinear) lie on the x-axis of the sidereal frame, while the remaining two are equidistant from the two main bodies and symmetrical with respect to the x-axis. Their location is showed in Fig. C.2.

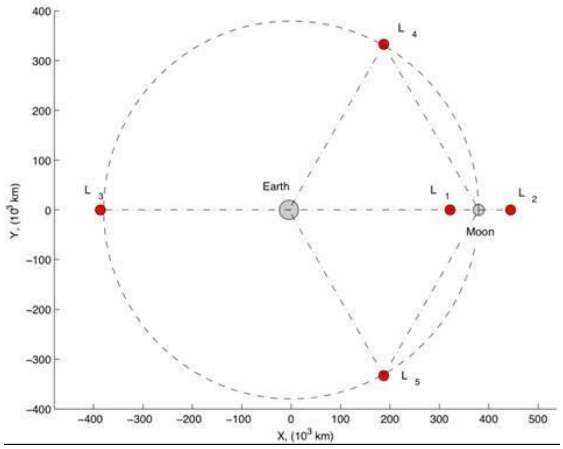

Figure C.2: Libration points in the Earth-Moon CR3BP [27].

Libration points are interesting for what concerns motion in their proximity, as they characterise islands of increased stability where it is customary to find closed solutions to the CR3BP itself. A spacecraft placed precisely at a Lagrange point (or either, on a closed periodic orbit) will remain there indefinitely, as long as a perturbation occurs causing it to drift away. The triangular points L_4 and L_5 are dynamically stable, so any perturbed particle remain in their vicinity. On the contrary the collinear points L_1, L_2 and L_3 are saddle equilibrium points.
At this stage, all the ingredients are given to explain the halo orbit concept. It is a periodic, three-dimensional orbit associated with one of the L_1, L_2 or L_3 Lagrange points in a three-body problem. Physically, these result comes from an interaction between the gravitational pull of the two planetary bodies and the Coriolis and centrifugal force on the considered spacecraft. A particular type of halo orbit that is taking hold in the new Moon exploration era is the near-rectilinear halo orbit (NRHO), that represents a theoretical solution of the CR3BP. Near-rectilinear means that some segments of the orbit have a greater curvature than those of an elliptical orbit of the same maximum diameter, and other segments have a curvature less than that of an elliptical orbit of the same maximum diameter (taking maximum diameter as that of the smallest circle that contains the whole of the orbit). The CAPSTONE mission, launched in 2022, is an example of the first spacecraft to use such orbit in cislunar space.

Bibliography

[1] Christopher T. Rodenbeck et al. «Microwave and Millimeter Wave Power Beaming». In: *IEEE Transactions on Antennas and Propagation* 69.10 (2021), pp. 5701–5717. DOI: 10.1109/TAP.2021.3084205 (cit. on p. 1).

[2] Henri Barde. «A Power Engineer View on Space Based Solar Power». In: *2023 13th European Space Power Conference (ESPC)*. 2023, pp. 1–11. DOI: 10.1109/ESPC59009.2023.10298124 (cit. on p. 4).

[3] Vahraz Jamnejad and Arnold Silva. «Microwave Power Beaming Strategies for Fractionated Spacecraft Systems». In: *Jet Propulsion Laboratory* (2021) (cit. on p. 4).

[4] Harry W. Jones. «The Recent Large Reduction in Space Launch Cost». In: *Proceedings of the 48th International Conference on Environmental Systems*. ICES-2018-81. NASA Ames Research Center, Moffett Field, CA, 94035-0001. Albuquerque, New Mexico: NASA Ames Research Center, July 2018 (cit. on p. 5).

[5] European Commission. *The European Green Deal*. Accessed: 2024. URL: https://commission.europa.eu/strategy-and-policy/priorities-2019-2024/%20story-von-der-leyen-commission/european-green-deal_en (cit. on p. 5).

[6] Politecnico di Milano. *Course Notes: Spacecraft Attitude Dynamics*. Prof. Franco Bernelli Zazzera. Part 1: Attitude dynamics and kinematics (cit. on p. 8).

[7] A.W. Rudge, K. Milne, A.D. Olver, and P. Knight. *The Handbook of Antenna Design*. Vol. 1. IEE Electromagnetic waves series 15, 2000 (cit. on pp. 13, 20, 27).

[8] *Polarization - EM Waves and Antennas*. URL: https://www.antenna-theory.com/basics/polarization.php (visited on 05/28/2024) (cit. on p. 20).

[9] Leehwan Hwang, Jongho Jeong, Cheolyoung Go, Philippe Gentet, Jungho Kim, Soonchul Kwon, and Seunghyun Lee. «Verification of Polarization Matching on the Hologram Recording Plane for the Implementation of an Optimized Digital Hologram Printing System». In: *Frontiers in Physics* (Apr. 2022). DOI: 10.3389/fphy.2022.857819 (cit. on p. 21).

[10] Geoffrey A. Landis. *Photovoltaic Receivers for Laser Beamed Power in Space*. Tech. rep. Prepared for Lewis Research Center Under Contract NAS3 - 25266. Sverdrup Technology, Inc., Lewis Research Center Group, Brook Park, Ohio: NASA Contractor Report 189075, Dec. 1991 (cit. on p. 27).

[11] Scott R. Starin and John Eterno. *Attitude Determination and Control Systems*. Document ID: 20110007876. NASA, 2011 (cit. on p. 28).

[12] S.A. Pourmousavi, Ratnesh K. Sharma, and Babak Asghari. «A Framework for Real-Time Power Management of a Grid-Tied Microgrid to Extend Battery Lifetime and Reduce Cost of Energy». In: *IEEE Transactions on Industrial Informatics* (2011) (cit. on p. 30).

[13] The MathWorks, Inc. *MATLAB*. Version R2019a. The MathWorks, Inc. Natick, Massachusetts, 2023. URL: https://www.mathworks.com/products/matlab.html (cit. on p. 32).

[14] *General Mission Analysis Tool (GMAT)*. Software. Accessed: June 2024. 2021. URL: https://gmat.sourceforge.io/ (cit. on p. 36).

[15] Leandro Zardaín, Ariadna Farrés, and Anna Puig. «High-fidelity modeling and visualizing of solar radiation pressure: A framework for high-fidelity analysis». In: (2021). Preprint. Accessed: June 25, 2024. DOI: AAS20-481 (cit. on p. 36).

[16] UK Solar System Data Centre. *MSISE-90 (Mass Spectrometer - Incoherent Scatter) Model of the Upper Atmosphere*. Website. Accessed: June 25, 2024. 2024. URL: https://www.ukssdc.ac.uk/ (cit. on p. 37).

[17] Luyuan Xu. *How China's lunar relay satellite arrived in its final orbit*. June 2018. URL: https://www.planetary.org/articles/20180615-queqiao-orbit-explainer (cit. on p. 60).

[18] European Space Agency. *ESA - European Space Agency*. https://www.esa.int/. Accessed: 2024-07-09 (cit. on p. 62).

[19] Todd Ely. «Stable Constellations of Frozen Elliptical Inclined Lunar Orbits». In: *The Journal of the Astronautical Sciences* 53.3 (July 2005), pp. 301–316. DOI: 10.1007/BF03546355 (cit. on p. 62).

[20] phys. *Bizarre Lunar Orbits*. Retrieved July 1, 2024, from https://phys.org/news/2006-11-bizarre-lunar-orbits.html. 2006 (cit. on p. 63).

[21] Matthew Peters, Victor Rossin, Matthew Everett, and Erik Zucker. «High Power, High Efficiency Laser Diodes at JDSU». In: *JDSU Corp.* () (cit. on p. 64).

[22] Yao Xiao, Jun Wang, Heng Liu, Pei Miao, Yudan Gou, Zhicheng Zhang, Guoliang Deng, and Shouhuan Zhou. «Multi-junction cascaded vertical-cavity surface-emitting laser with a high power conversion efficiency of 74%». In: *Light: Science & Applications* 13 (2024), p. 60. ISSN: 2047-7538. DOI: 10.1038/s41377-024-01403-7. URL: https://www.nature.com/lsa (cit. on p. 64).

[23] Debra M. Hurwitz, James W. Head, and Harald Hiesinger. «Lunar sinuous rilles: Distribution, characteristics, and implications for their origin». In: *Planetary and Space Science* 79-80 (2013). Received 28 May 2012, Revised 18 October 2012, Accepted 31 October 2012, Available online 10 January 2013, pp. 1–38 (cit. on p. 83).

[24] Knowino. *Earth's orbit*. June 14, 2024. URL: https://www.theochem.ru.nl/~pwormer/Knowino/knowino.org/wiki/Ecliptic.html (cit. on p. 86).

[25] B. Fiedler, K. Gröger, and J. Sprekels. *Dynamics of the Three Body Problem*. World Scientific Publishing Company, 2000. DOI: 10.1142/4469. URL: http://www.worldscientific.com/worldscibooks/10.1142/4469 (cit. on p. 90).

[26] Robert Jedicke, Bryce T. Bolin, William F. Bottke, Monique Chyba, Grigori Fedorets, Mikael Granvik, Lynne Jones, and Hodei Urrutxua. «Earth's Minimoons: Opportunities for Science and Technology». In: *Frontiers in Astronomy and Space Sciences* 5 (May 2018), p. 13. DOI: 10.3389/fspas.2018.00013 (cit. on p. 91).

[27] Deepak Gaur and Mani Shankar Prasad. «Communication Relay Satellites Constellation Assessment for Future Lunar Missions». In: *Journal of Aerospace Engineering* (2021) (cit. on p. 92).